# Evolution of the Earth's Ring Current during Geomagnetic Storms

by

Eric W Grimes

A thesis submitted to the Graduate Faculty of
Auburn University
in partial fulfillment of the
requirements for the Degree of
Master of Science

Auburn, Alabama
December 8, 2012

Keywords: Space Physics, Ring Current, Energetic Neutral Atoms, Magnetospheric Plasmas

Approved by

Joseph Perez, Chair, Professor of Physics
Yu Lin, Professor of Physics
Edward Thomas, Professor of Physics

Abstract


We examine the evolution of the ring current during the main and early recovery phases of five geomagnetic storms, three driven by co-rotating interaction regions (CIRs) in the solar wind and two driven by interplanetary coronal mass ejections (ICMEs), also known as solar flares. The equatorial energy density profiles of 5–65 keV ions are calculated from deconvolved energetic neutral atom (ENA) images from the Two Wide-Angle Imaging Neutral-Atom Spectrometers mission. The energy density in the ring current is enhanced by almost a factor of 2 and stretches from post-midnight to dusk immediately following injections identified by in situ measurements and increases in the auroral electrojet index. The energy density then drops back to pre-injection levels within 1–2 h. We also find that, for CIR-driven storms, there are often two peaks in the energy density following the injection, one at midnight and one close to dusk. We present the spectra for these peaks to show they contain different ion populations. For the ICME-driven storms, only one peak is observed in the energy density near midnight. For all storms in this thesis, the equatorial peak in energy density is thought to be mostly observed through low altitude emissions, owing to the higher geocoronal density at lower altitude. To better quantify where the peak in the ion distribution is being observed in the ENA images, we also show the equatorial pitch angle anisotropy in the ions for the ICME-driven storms. For both the CIR and ICME-driven storms, the asymmetry of the ring current observed is found to agree with previous *in situ* and simulation studies.

Acknowledgments

First and foremost, I have to thank Dr. Joseph Perez, my faulty advisor and mentor for the last six years (two as an undergraduate, four as a graduate student), for the tremendous support and educational experience he has provided. Six years ago, I did not know what magnetospheric plasmas were; now, I'm an expert. I can only hope that future mentors are half as helpful, understanding and excited about our work as he has been.

I would also like to acknowledge Dave McComas, Jerry Goldstein and Phil Valak (all of Southwest Research Institute), as well as the rest of the TWINS science team for all of the support, guidance and many fruitful discussions over the last six years.

I would also like to thank S. Kokubun (STELAB Nagoya University, Japan) and T. Nagai (Tokyo Institute of Technology) for the use of the Geotail magnetic field data; H. Singer (NOAA SEC) for the GOES magnetic field data; J. H. King, N. Papatashvilli (AdnetSystems, NASA GSFC, CDAWeb, OMNI), and N. Ness (Bartol Research Institute) for the ACE interplanetary magnetic field data, as well as WDC Kyoto for the use of AE, SYMH and ASYMH indices.

Table of Contents

# List of Figures

# 1. Introduction

Geomagnetic storms during the declining phase of the solar cycle are predominately driven by corotating interaction regions (CIRs) originating at coronal holes on the Sun [*Krieger et al.,* 1973*; Tsurutani et al*., 2006]. Due to the different driving mechanisms in the solar wind, these storms are inherently different than their interplanetary coronal mass ejection (ICME) counterparts. CIRs produce weak storms with recovery phases that typically last from several days to several weeks. These long recovery phases are due to nonlinear Alfven waves that follow the fast stream interface [*Tsurutani and Gonzalez*, 1987]. Protons are injected into the magnetosphere by these Alfven waves when the oscillating $B_z$ component of the interplanetary magnetic field (IMF) becomes negative [*Sandanger et al*., 2005]. *Tsurutani et al*. [2006] found a one to one relationship between southward IMF $B_z$, decreases in Dst and AE increases during the recovery phase of a CIR storm, suggesting that the ring current is directly influenced by the interplanetary Alfven waves through High-Intensity Long-Duration Continuous AE Activity (HILDCAA) events. *Denton et al*. [2006] and *Borovsky and Denton* [2006] use a superposed epoch analysis to study the different responses of the magnetosphere to these different drivers. Most notably, they find that geomagnetic storms driven by CIRs have a less dense, but hotter plasma sheet than that of ICMEs.

The peak in ring current pressure is thought to reside in the dusk-midnight region. For example, *Studemann et al*. [1987] found that protons with energies up to ~140 keV are significantly enhanced in the dusk region as compared to dawn using in-situ data from a few hours after onset of a geomagnetic storm. Using a statistical analysis of in-situ measurements

1

from ISEE, AMPTE/CCE and Polar, *Le et al.*[2004] and *Lui* [2003] also found the same local time asymmetry with higher plasma pressures in the dusk-midnight region. *Korth et al.* [1999], *Denton et al.* [2005] and *Zhang et al.* [2006] all used data from the magnetospheric plasma analyzer (MPA) instrument onboard LANL geosynchronous satellites to show this local time asymmetry also exists in proton density and temperature at geosynchronous orbit. *Zhang et al.* [2007] also observed an asymmetrical ring current using simulations of plasma pressure during a moderate storm. Linear inversions of ENA observations by *Brandt et al.* [2002], however, showed a peak in plasma pressure in the post-midnight region. The authors suggested this effect could be due to shielding electric field created in the ring current or by a skewed convection pattern due to IMF $B_y$. *Ebihara and Fok* [2004] used the Comprehensive Ring Current Model (CRCM) to show that this post-midnight peak in plasma pressure could be due to a deformation of the convection electric field due to shielding and/or due to the local time dependence of the plasma sheet density, as well as a skewed convection pattern due to IMF $B_y$. More recently, *Buzulukova et al.* [2010] used CRCM to verify that overall convection strength and electric field skewing due to shielding are the most important factors behind post-midnight enhancements.

*Iyemori and Rao* [1996] found that the recovery of Sym-H is accelerated just after substorm onset during the recovery phase of storms. This is counterintuitive, as the substorm should inject fresh plasma into the ring current which should lead to a more intense ring current and decrease Sym-H. Both *Lui et al.* [2001] and *Ohtani et al.* [2005] showed that ring current ENA intensity increases after substorm onset, which is evidence of fresh plasma being injected. *Siscoe and Petscheck* [1997] suggested that the increase in Sym-H is due to the reduction of the cross tail current just after substorm onset. *Ohtani et al.* [2001] used a statistical study to show that the geosynchronous magnetic field tends to dipolarize near minimum Sym-H and the

subsequent recovery of Sym-H is due to the reduction of the cross tail current, as suggested by *Siscoe and Petscheck* [1997]. *Ohtani et al.* [2005] showed this same counterintuitive relationship between Sym-H and ring current strength using ENA intensities measured by the high-energy neutral atom (HENA) imager.

The Two Wide-angle Imaging Neutral-atom Spectrometers (TWINS) mission is a mission of opportunity through the NASA Explorer program to simultaneously observe energetic neutral atoms (ENAs) created when positively charged ions charge exchange with cold neutral hydrogen (at high altitudes) and cold neutral oxygen (at low altitudes) in the magnetosphere. TWINS observes ENAs from 1-100 keV with a 4°x4° degree angular resolution and completes a single sweep image in just over a minute. A full description of the instrumentation can be found in *McComas et al.* [2009a; 2012].

Prior to attempting to extract the ion distribution, the TWINS images are statistically smoothed using a technique described in detail in Appendix A of *McComas et al.* [2012] and previously applied successfully to ENA images from IBEX [*McComas et al.*, 2009b] and TWINS [*Valek et al.*, 2010]. The equation for the line-of-sight integral of the $\alpha^{th}$ pixel of an ENA image can be expressed as:

$$d_\alpha = \int \int \int I(x,v,t)\sigma_{ex}(E)n(x)R_\alpha(x)d^3x$$

Where $d_\alpha$ is the ENA intensity, *I(x,v,t)* is the ion intensity, *n(x)* is the neutral hydrogen density, $\sigma_{ex}$ is the energy dependent charge-exchange cross section of protons with neutral hydrogen and neutral oxygen [*Barnett*, 1990], and $R_\alpha$ is the response function of the instrument. For each point along the line-of-sight, the neutral hydrogen density is estimated using the model by *Østgaard et al*. [2003] and the geomagnetic field is modeled using *Tsyganenko et al.* [2005]. The ion intensities are then extracted from the ENA images using an inversion technique based on

*Wahba* [1990] in which the intensity is expanded in terms of tri-cubic B-splines [*deBoor*, 1978]. The expansion coefficients, $a_{i,j,k}$, are defined by the expression

$$I(r, \varphi, \cos \psi) = \sum_i \sum_j \sum_k a_{i,j,k} S_i(r) P_j(\varphi) S_k(\cos \psi)$$

where $S_i(r)$ are the radial splines, $P_j(\varphi)$ are periodic, angular (MLT) splines, and $S_k(cos\psi)$ are the cosine of the equatorial pitch angle splines are obtained by solving a set of integral equations obtained from the minimization requirement,

$$\delta(\chi^2 - \lambda P) = 0$$

The $\chi2$,

$$\chi^2 = \frac{1}{N} \sum_{\alpha=1}^{N} \frac{(d_\alpha - c_\alpha)^2}{\sigma_\alpha^2}$$

where $\sigma_\alpha$ is the uncertainty in the $\alpha^{th}$ pixel and $c_\alpha$ is the ENA intensity in the $\alpha^{th}$ pixel,

$$c_\alpha = \sum_i \sum_j \sum_k D_{\alpha\{i,j,k\}} a_{i,j,k}$$

imposes the constraint of fitting the data and the penalty function, *P*, requires that the solution be as smooth as possible. The expression for *P* is given in *Perez et al.*[2001]. Qualitatively, it means the smallest possible second derivative while still fitting the data. Thus, the λ parameter represents the balance between fitting the data and smoothness of the data. $D_{\alpha,\{i,j,k\}}$ is the design matrix for the $\alpha^{th}$ pixel,

$$D_{\alpha,\{i,j,k\}} = \int \int \int \sigma_{ex}(E) n(x) S(r) P(\varphi) S(\cos \psi) R(x) d^3 x$$

To extract statistically significant information from the data, we then require that $\chi2=1$. This technique, described in detail by *Perez et al.* [2012], allows us to calculate the equatorial

distribution of the ions producing ENAs in the ring current for each instrument with minimal prior information about the underlying ion distribution.

In the next section of this thesis, we examine the evolution of the terrestrial ring current during three CIR-driven geomagnetic storms using 5-30 keV ion intensities deconvolved from the TWINS-1 ENA imager. The first event examined is during the main phase of a storm on July 12, 2008, just prior to a dipolarization signature measured in the midnight region and subsequently near dusk by GOES magnetometers at geosynchronous orbit. The equatorial energy density for 5-30 keV ions peaks across the night side ring current in the time interval following the injection inferred by the dipolarization observed at geosynchronous orbit. Two hours after the injection, the energy density has dropped off significantly and is peaked near midnight. The ion spectra of this peak shows a Maxwellian peaked at 10 keV. The second event examined is during the early recovery phase of a storm on August 10, 2008. A dipolarization is observed by GOES-11 near dusk just before being measured by GOES-12 near midnight. The equatorial energy density increases by a factor of two during the time frame following the presumed injection. The third event examined, September 4, 2008, is also during the early recovery phase. Data for this event includes Geotail observations of an earthward plasma injection in the plasma sheet, followed by GOES observations of a dipolarization signature near midnight. Again, the deconvolved energy density increases by a factor of two immediately following the injection and then decreases. In each case during the early recovery phase, we observe two peaks in the energy density after the injection, the first being at midnight and the second towards dusk.

In section 3 of this thesis, we examine the evolution of the terrestrial ring current during two ICME-driven geomagnetic storms using 5 - 65 keV ion intensities deconvolved from the TWINS-1 and TWINS-2 ENA imagers. The first event shown is during the late main and early

recovery phases of a storm on March 11, 2011. A substorm signature is inferred by an increase

(to greater than 1000 nT) in the AE index towards the end of the main phase of the storm. This

peak in AE index corresponds to a peak in the asymmetric component of the ring current as

observed through the ASym-H index. The equatorial plasma energy density is strongly

asymmetric, with a peak near midnight. This peak corresponds to a field aligned distribution

observed in the equatorial pitch angles. The field aligned distribution is likely the result of the

spacecraft viewing geometry. The second event shown in section 3 is during the early recovery

phase of a storm on May 28, 2011. Again, we infer substorm by a peak in the AE index.

Interestingly, while the 15 keV ENA intensities peak during the beginning of the observations,

the 5-65 keV equatorial energy density tends to follow the AE index. Also interestingly, a drop-

off in low altitude emissions observed emanating from the southern hemisphere is found to

correspond to a less symmetric ring current during the latter part of the interval. This asymmetry

is found to agree with a ~50 nT increase in the asymmetric component of the ring current as seen

in the ASym-H index.  As with CIR-driven storms, the peak in energy density tends to follow the

substorm signatures.

## 2. Geomagnetic Storms Driven by Co-rotating Interaction Regions (CIRs)

The geomagnetic storms presented in this section occurred during three successive months and are due to a 27-day recurring CIR structure in the solar wind. The structure in the solar wind can be further identified by the Alfven waves following the stream interface which drive the oscillating $B_z$ component of the interplanetary magnetic field. The interval of time for these events was chosen at times of highest geomagnetic activity so as to have the highest counts into the instrument. The storms driven by this CIR structure are only small to moderate sized storms as defined by *Gonzalez et al.* [1994].

### 2.1 The 12 July 2008 Event

Figure 1 shows 5-min averages of IMF $B_y$, $B_z$, the auroral electrojet index (AE) and Sym-H index provided by OMNI for the day of July 12, 2008 (left). The oscillatory nature of IMF $B_z$ about zero is clear in the recovery phase late in the day. The vertical lines on the left plot indicate the time interval observed by TWINS-1 and we zoom in on this interval using 1-min OMNI data on the right. The IMF conditions are time shifted to the magnetopause by OMNI. IMF $B_y$ is mostly negative for the entire interval, with slight positive excursions around 0335 UT and 0530 UT. IMF $B_z$ is also mostly negative for this interval, with a 10-min northerly excursion at 0430 UT. The AE index is elevated for the interval, with peaks around 900 nT at 0330 UT and 0545 UT. Sym-H shows that the time of interest is at the beginning of the main phase of the storm and goes from positive to negative at 0400 UT, dropping to almost -30 nT for the interval.
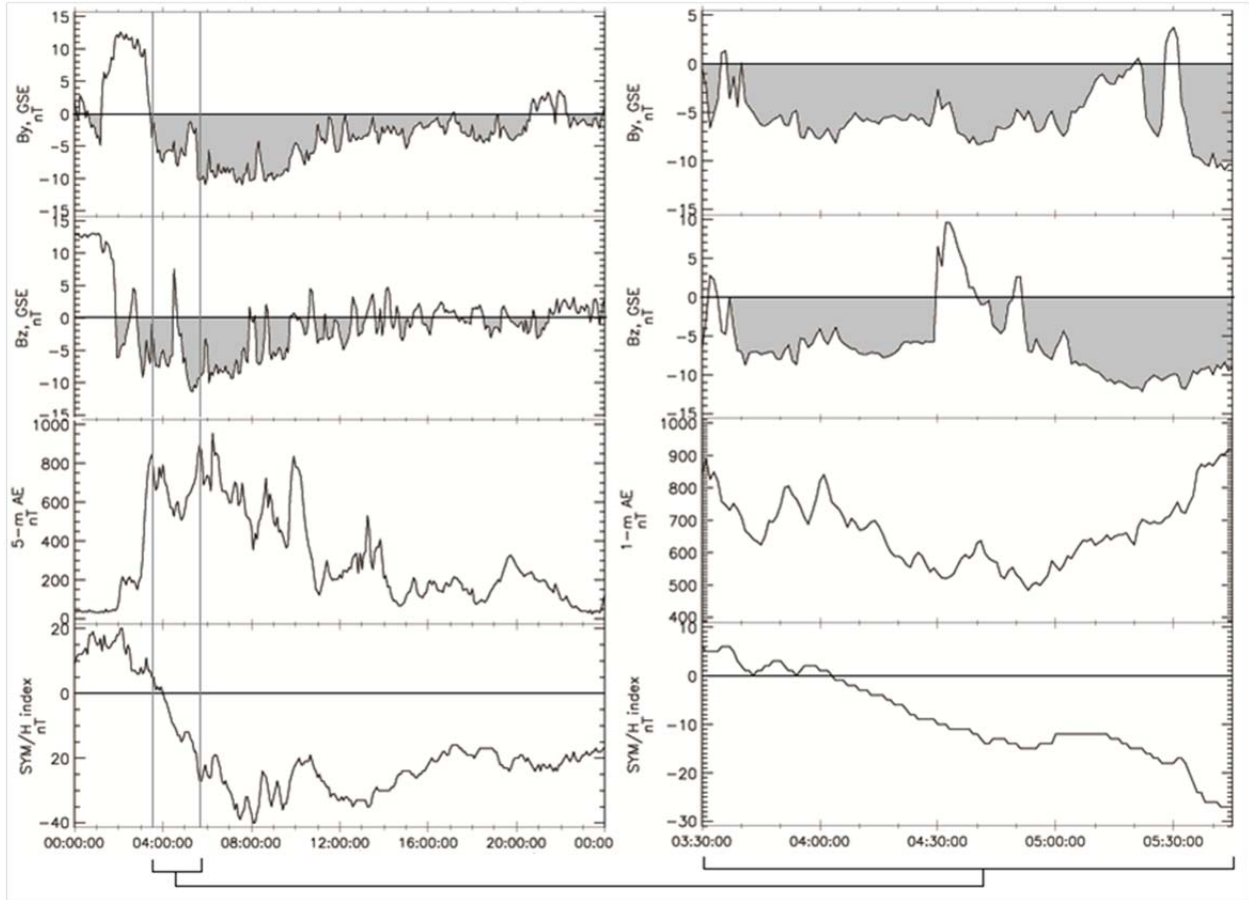
**Figure 1: The IMF By, Bz and AE, Sym-H indices for July 12, 2008 (left) and 0330 UT-0545 UT (right).**

Figure 2 shows the 10 keV ENA images for 0330 UT - 0545 UT. The images are 24 sweep, 33 minute averages projected onto a skymap view with dipole field lines at McIlwain L shells of L=4 and L=8. The red and purple L-shells indicate the sunward and duskward directions, respectively. During 0330-0404 UT, the TWINS-1 spacecraft is at R= ~5 $R_e$, 52 degrees latitude and is viewing from post-dawn in the northern hemisphere. Strong low altitude emissions are observed just off the Earth's limb from both the northern and southern hemispheres. High altitude emissions are observed at midnight around the L=4 dipole L-shell. From 0404-0437 UT, TWINS-1 has moved to R=5.6 $R_e$ , 57 degrees latitude. The ENAs produced at low altitude have decreased by ~25% and are still observed emanating from both

8

hemispheres. By 0438-0511 UT, the spacecraft has moved to R=6.1 $R_e$, 60 degrees latitude and no longer sees the low altitude emissions from the southern hemisphere. Both high altitude and low altitude ENAs have increased by ~10%. From 0511-0545 UT, the spacecraft is at R=6.5 $R_e$, 63 degrees latitude. Low altitude emissions have increased by another ~15%, almost reaching the ENA flux observed during the 0330-0404 UT period.
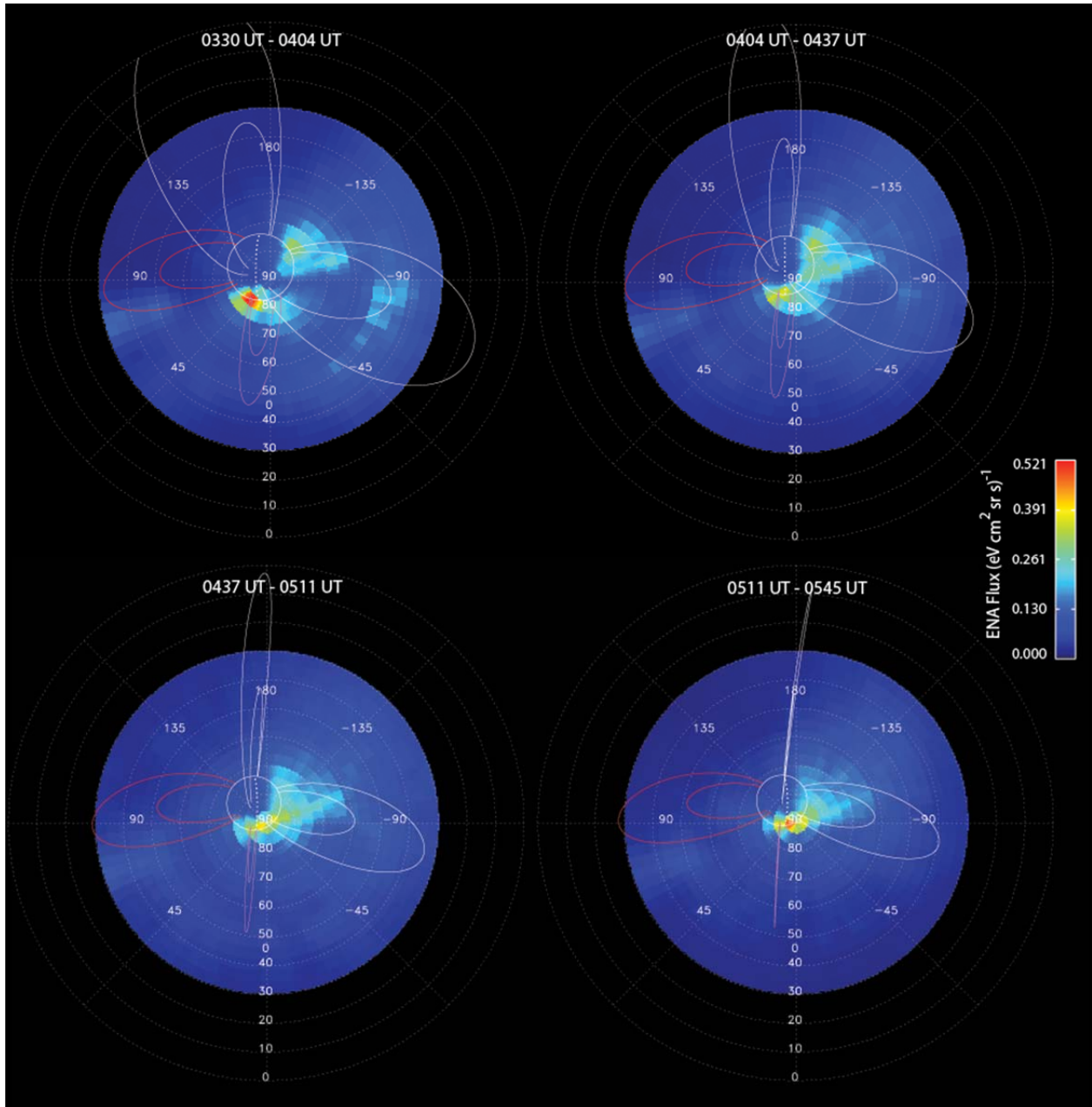


**Figure 2: TWINS-1 10 keV ENA flux for July 12, 0330-0545 UT.**
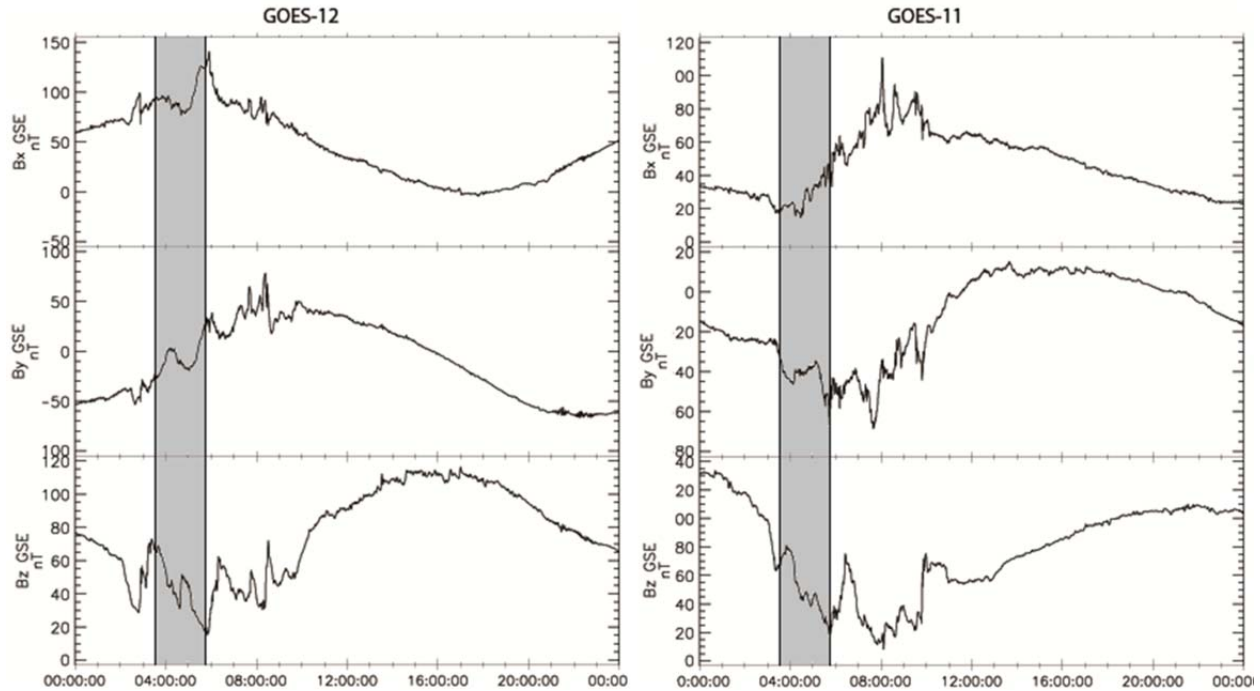
**Figure 3: GOES-12 and GOES-11 geomagnetic field data for July 12, 2008.**

GOES-11 (right) and GOES-12 (left) magnetometer data are presented in Figure 3, with GOES equatorial positions shown in Figure 4. A dipolarization signature, a sharp increase in $B_z$, is measured at GOES-12 in the pre-midnight region just before 0300 UT. The dipolarization signature is then measured by GOES-11 near dusk at 0330 UT. A second, much smaller dipolarization signature is measured by GOES 12 close to 0445 UT. Both GOES-11 and GOES-12 continue to observe dipolarization signatures on the night side for several hours after the interval of interest.
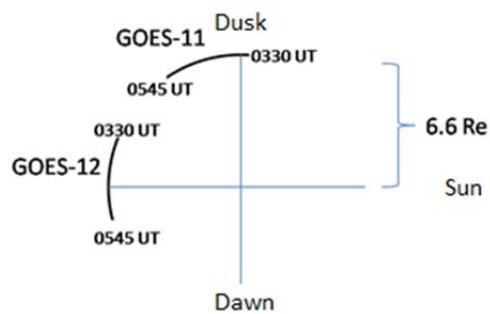


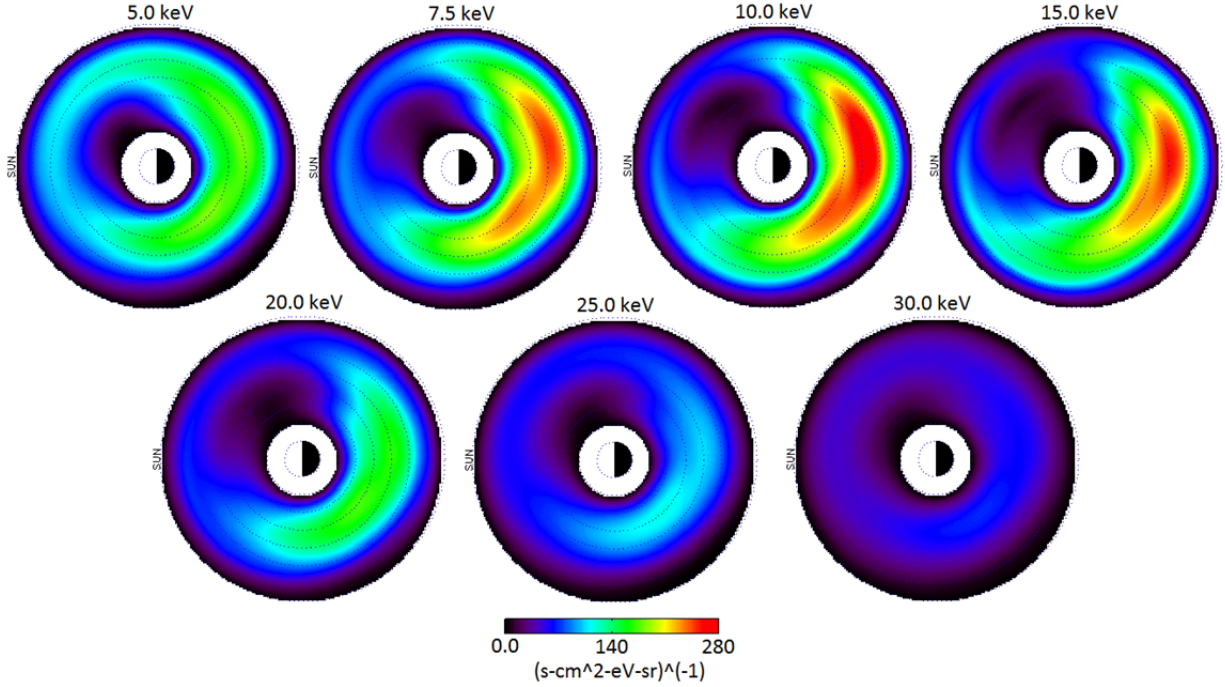**Figure 4: GOES equatorial spacecraft locations for 0330 UT - 0545 UT on July 12, 2008.**

**Figure 5: Equatorial intensity averaged over pitch angle for 5-30 keV ions on July 12, 2008, 0511UT - 0545UT.**

As an example of the energy dependent global images during this period, the deconvolved 5-30 keV equatorial ion intensities for 0511-0545 UT are presented in Figure 5. The sunward direction is to the left in all images. We observe a single peak in ion intensity at 10 keV near midnight. The peak in ion intensity at lower energies is slightly more dawnward than the peak in higher energies, consistent with gradient and curvature drift of the ions [*Ejiri et al.*, 1980; *Fok et al.*, 1996; *Kistler and Larson*, 2000]. Though, detailed analysis of the drift dynamics is beyond the scope of this paper.

In Figure 6, we present the time evolution of the spectra of the distribution at its peak intensity (R=5.3 R$_e$, MLT=0.0) through the entire interval. The spectra at midnight does not have a clear peak during the first period (0330-0404 UT), when the dipolarization is observed at geosynchronous. From 0404-0545 UT, the tail of the spectra gradually increases in slope, finally settling to a Maxwellian-like distribution during the final period (0511-0545 UT).
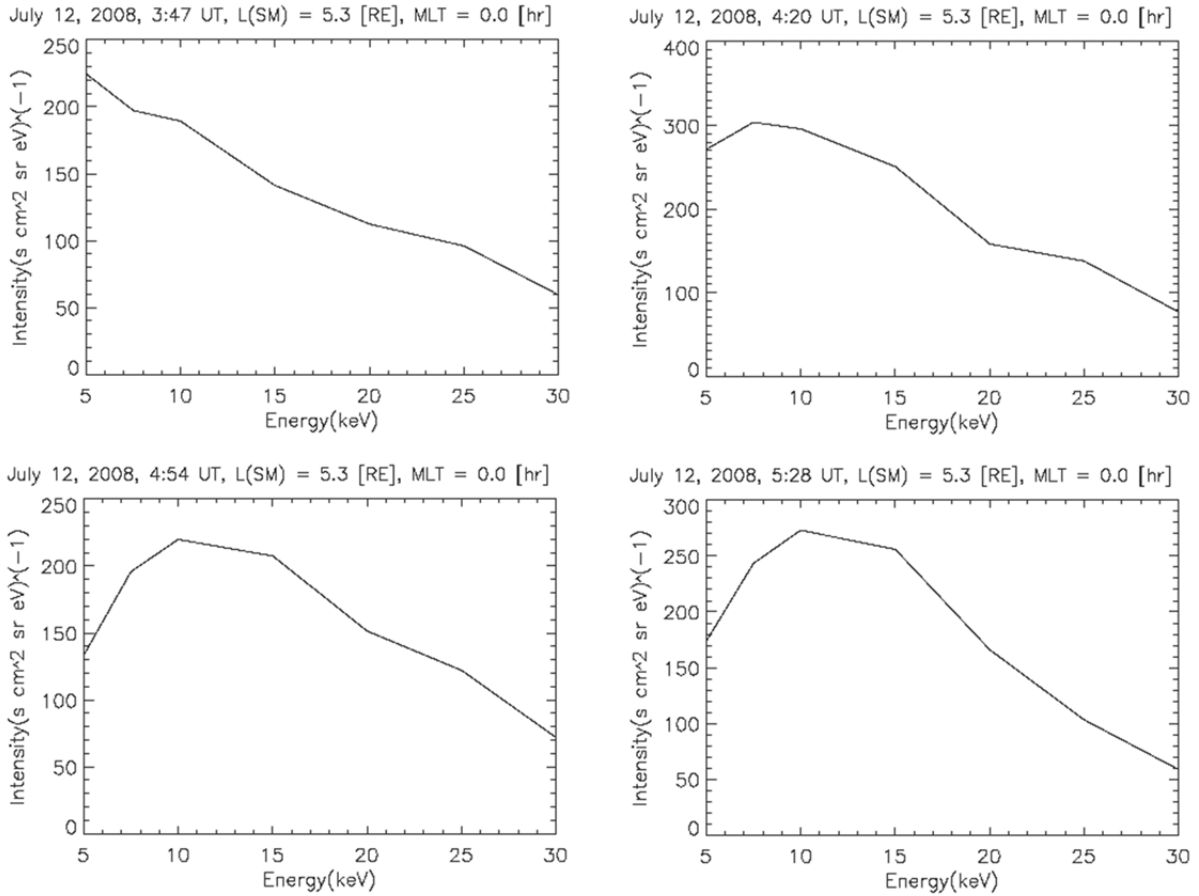
**Figure 6: Evolution of intensity spectra at R=5.3, MLT=0.0 (0330 UT - 0545 UT) on July 12, 2008.**

In Figure 7, we present equatorial energy density (5-30 keV) profiles calculated from the deconvolved ion intensities for this interval. The peak in energy density of the ring current begins in the pre-midnight region during 0330-0404 UT and spreads out in MLT during 0404-0437 UT. By 0437-0511 UT, the peak in ring current energy density has decreased in magnitude and spatial extent slightly and now extends from midnight to dusk. The energy density continues to fall in the next time interval and peaks at midnight. The magnitude of the peak in the energy density between 5 and 30 keV does not increase with falling Sym-H but rather rises and falls following dipolarization events observed at geosynchronous orbit.
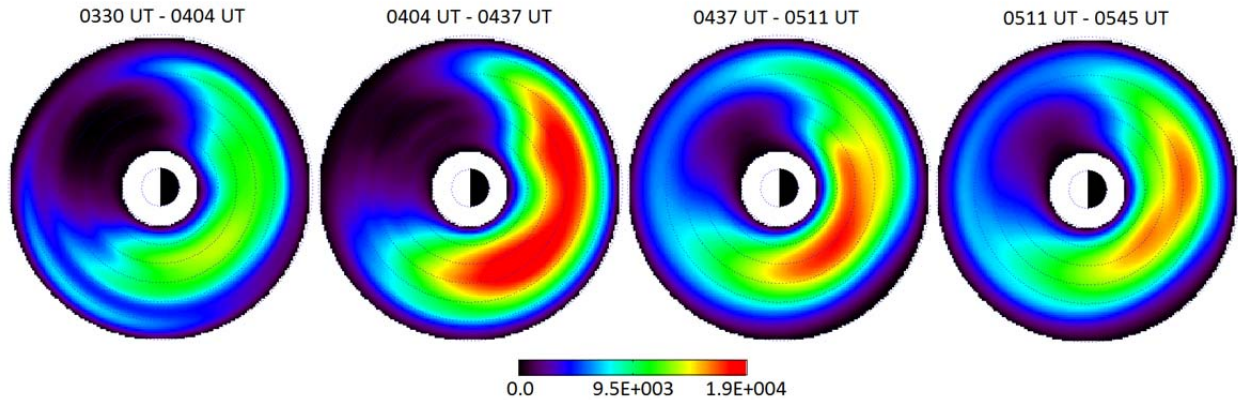
**Figure 7: Equatorial 5-30keV energy density profiles for July 12, 2008.**

2.2 The 10 August 2008 Event

Five minute averages of IMF $B_y$, $B_z$, AE and Sym-H provided by OMNI for the day of August 10, 2008 are presented in Figure 8 (left). Again, the vertical lines indicate the time interval observed by TWINS-1, and we zoom in on this interval using 1-min resolution OMNI data on the right. There are two large negative IMF $B_y$ regions in the interval, the first occurring between 0520 UT and 0600 UT and the second between 0620 UT and 0730 UT. IMF $B_y$ is also slightly negative for 15 minutes just after 0600 UT. IMF Bz is negative for most of the interval, with slight northerly excursions between 0600 UT and 0620 UT. AE peaks between 0520 UT and 0545 UT, reaching over 900 nT at times. AE then falls off to slightly above 200 nT before the end of the interval. Sym-H increases by 20 nT over the interval and is relatively flat during 0500-0530 UT and 0540-0620 UT. Both AE and Sym-H seem to be controlled by southward IMF $B_z$. Note that the time of interest is in the early recovery stage of the storm just after the minimum in Sym-H.
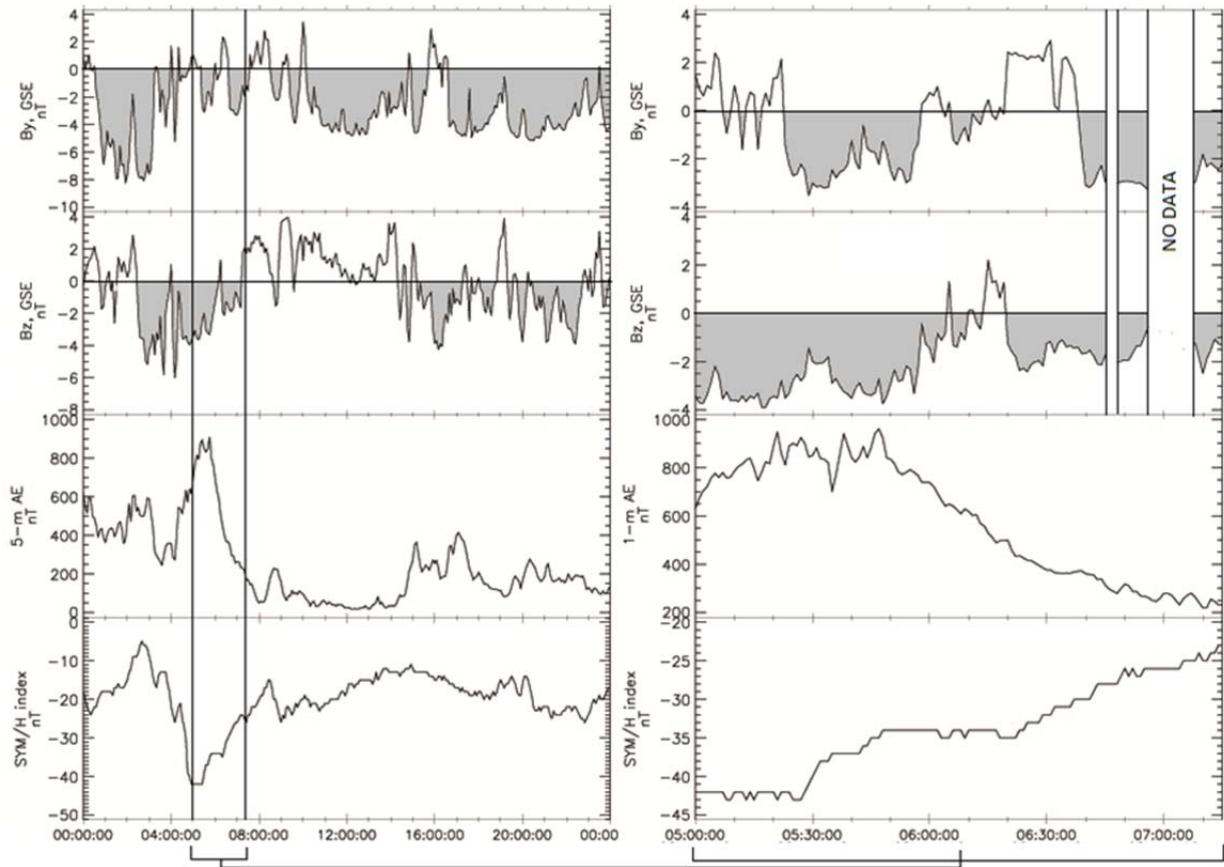
13

**Figure 8: The IMF By, Bz and AE, Sym-H indices for August 10, 2008 (left) and 0500 UT-0715 UT (right).**

The 10 keV ENA images for 0500-0715 UT are shown in Figure 9. Again, we use 24 sweep, 33 minute averages projected onto a skymap with the red and purple L shells indicating sunward and duskward directions. The TWINS-1 spacecraft is at R=7.1 $R_e$, 65.6 degrees latitude during 0500-0533 UT, viewing from dawn in the northern hemisphere. It progresses to R=6.7 $R_e$, 62.8 degrees latitude throughout the interval. During 0500-0533 UT, TWINS-1 observes the majority of 10 keV ENAs being produced as low altitude emissions. The ENAs from low altitude emissions peak during 0533-0607 UT and then fall off gradually until the end of the interval. We also observe a gradual increase in high altitude emissions directly from ring current ions

14

between midnight and dawn during 0500 UT and 0640 UT. The high altitude emissions appear
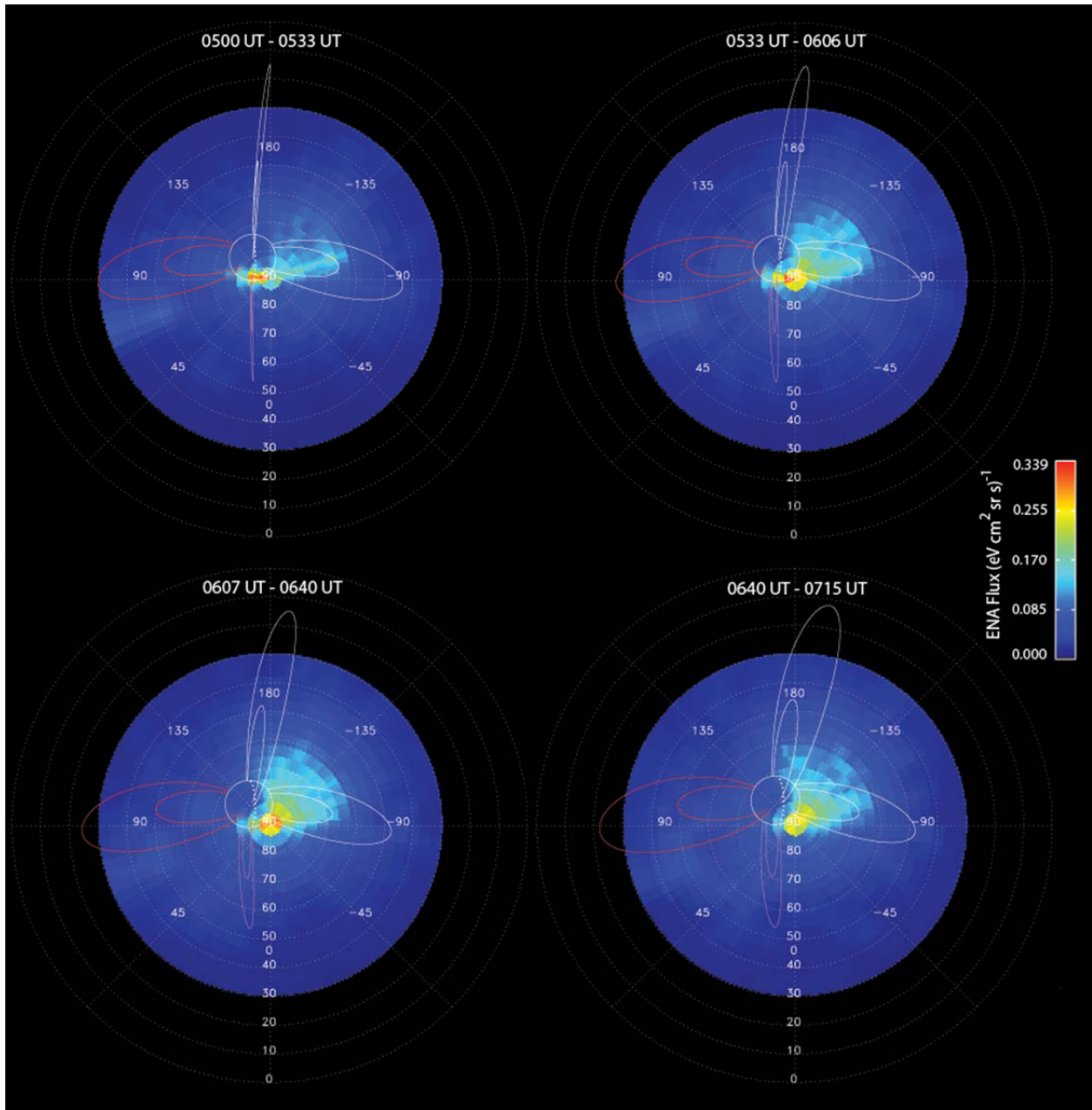to drop off during the 0640-0715 UT interval.



**Figure 9: TWINS-1 10 keV ENA flux for 0500 UT - 0715 UT on August 10, 2008.**

Figure 10 shows the geomagnetic field at geosynchronous orbit measured by GOES-12
(left) and GOES-11 (right) on August 10, 2008. The locations of the geosynchronous spacecraft

are shown in Figure 11. GOES-11 observes a dipolarization signature at 0500 UT near dusk.

GOES-12 observes a similar signature at 0530 UT just dawnward of midnight.
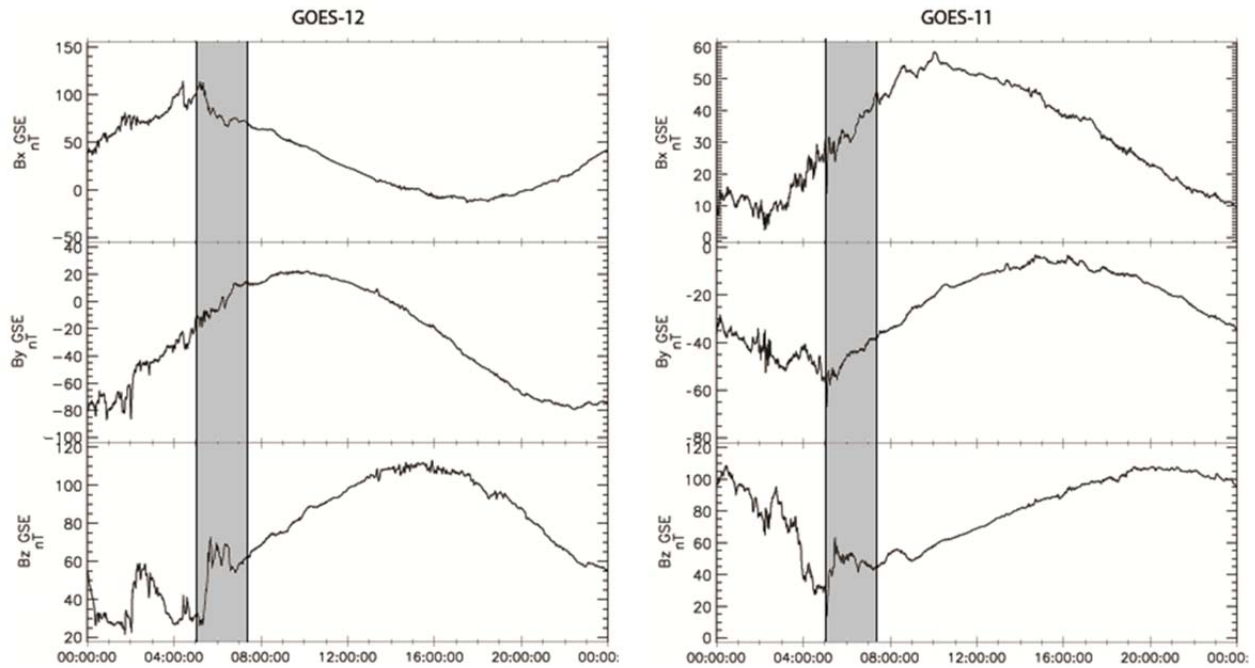


**Figure 10: GOES-12 (left) and GOES-11 (right) geomagnetic field data for August 10, 2008.**
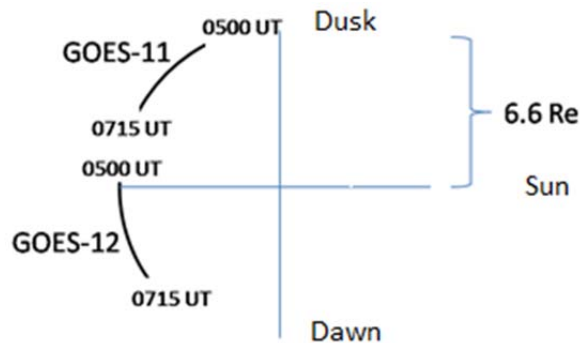


**Figure 11: GOES equatorial spacecraft locations for 0500 UT - 0715 UT on August 10, 2008.**

As an example of the energy dependent global images during this period, the 5-30 keV equatorial ion intensities for 0640-0715 UT are shown in Figure 12. We observe two peaks in the 10 keV ion intensity, one near midnight between L=3 and L=5 and one near dusk between L=6 and L=7. The spectra for these two peaks are shown in Figure 13. From the spectra, we

observe that these two locations contain different plasma populations. The spectra at midnight peaks at 10 keV while the spectra near dusk peaks at 15 keV.
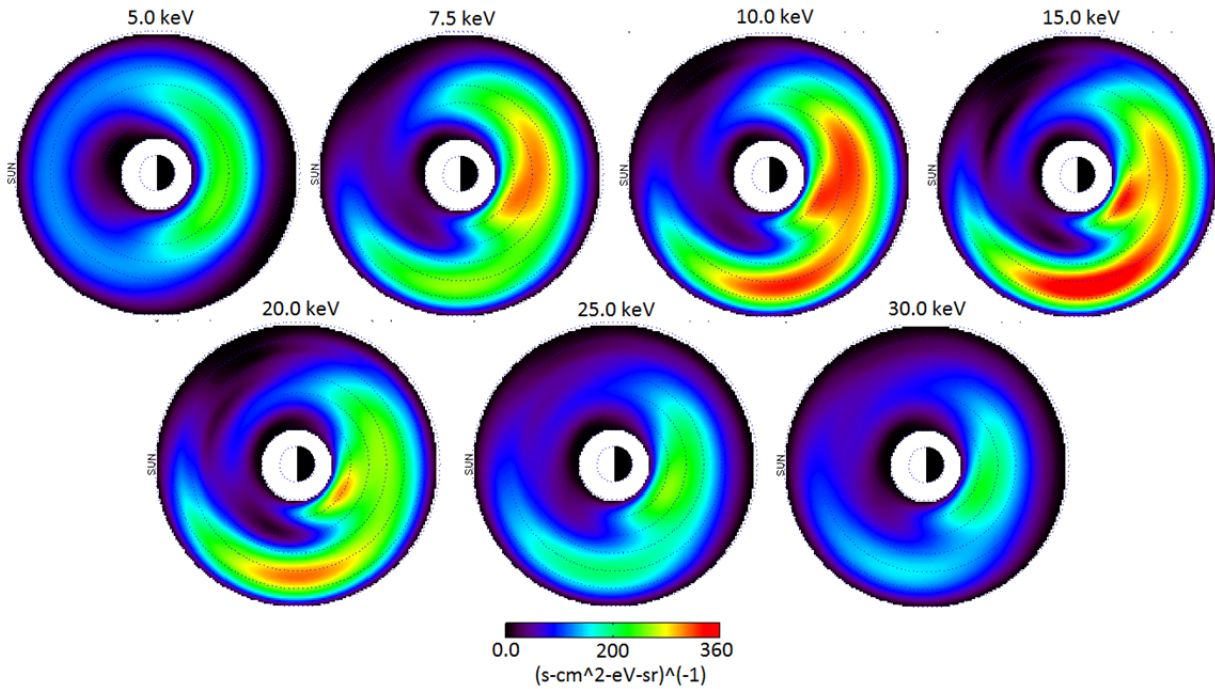


**Figure 12: Equatorial intensity averaged over pitch angle for 5-30 keV ions on August 10, 2008, 0640 UT - 0715 UT.**
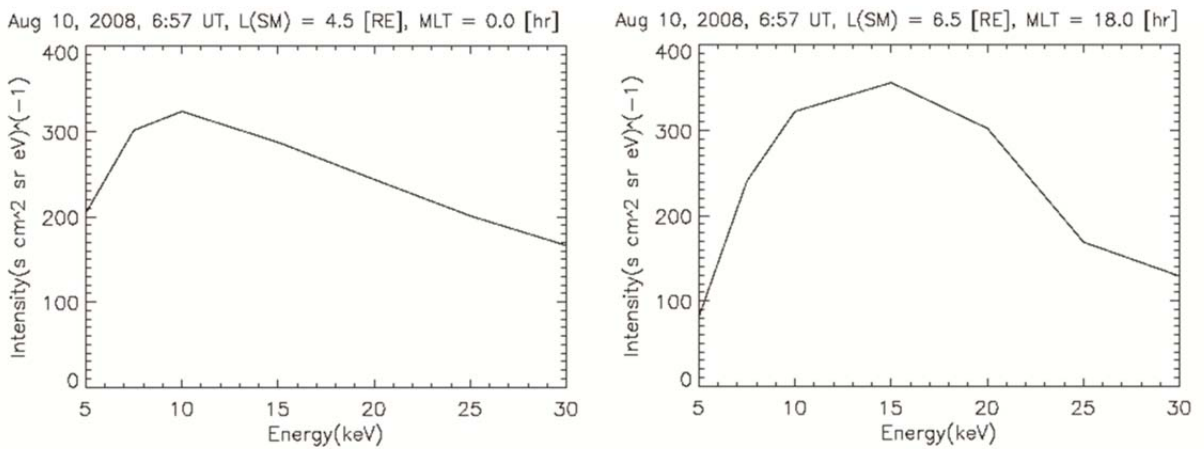


**Figure 13: August 10, 2008, 0640 UT - 0715 UT (a) 5-30 keV intensity spectra at R=4.5, MLT=0.0 and (b) R=6.5, MLT=18.**
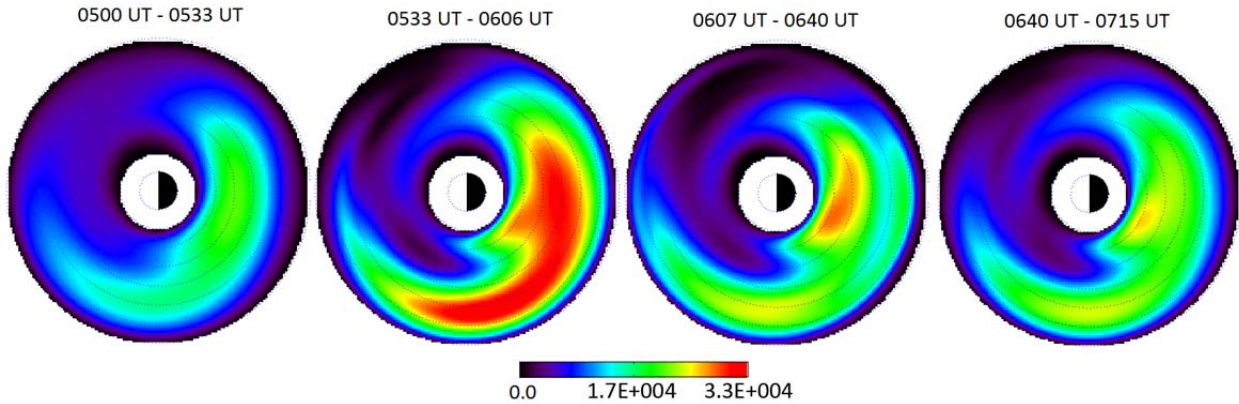
**Figure 14: 5-30keV equatorial energy density profiles for 0500 UT - 0715UT on August 10, 2008.**

The 5-30 keV equatorial energy densities are shown in Figure 14. The energy density is initially peaked in the pre-midnight region between L=3 and L=5 $R_e$. During 0533-0606 UT, the energy density increases by a factor of two as a result of the plasma injection inferred from geosynchronous measurements. This evolves into two peaks during 0607-0640 UT, one near midnight between L=3 and L=5 $R_e$ and one near dusk between L=6 and L=7 $R_e$. Both peaks then decrease in magnitude over the next hour while maintaining their spatial structure. Again the strength of the energy density between 5 and 30 keV seems to follow dipolarization.

2.3 The 4 September 2008 Event

Figure 15 (left) shows the IMF $B_y$ and $B_z$, as well as the AE and Sym-H indices for the day of September 4, 2008. The time of interest is marked by vertical lines and expanded on the right using 1-min resolution OMNI data. IMF $B_y$ is positive for the majority of the interval, with negative excursions at the beginning of the interval and from 0450-0520 UT. IMF $B_z$ is negative for most of the interval with a single northerly excursion at 0515 UT. The AE index is elevated for the entire interval, but steadily decreases from 1400 nT at 0325 UT to 500 nT. Sym-H reaches -67 nT just before 0400 UT, making this the strongest storm studied in this paper. Note that the time of interest is again in the early recovery phase of the storm.
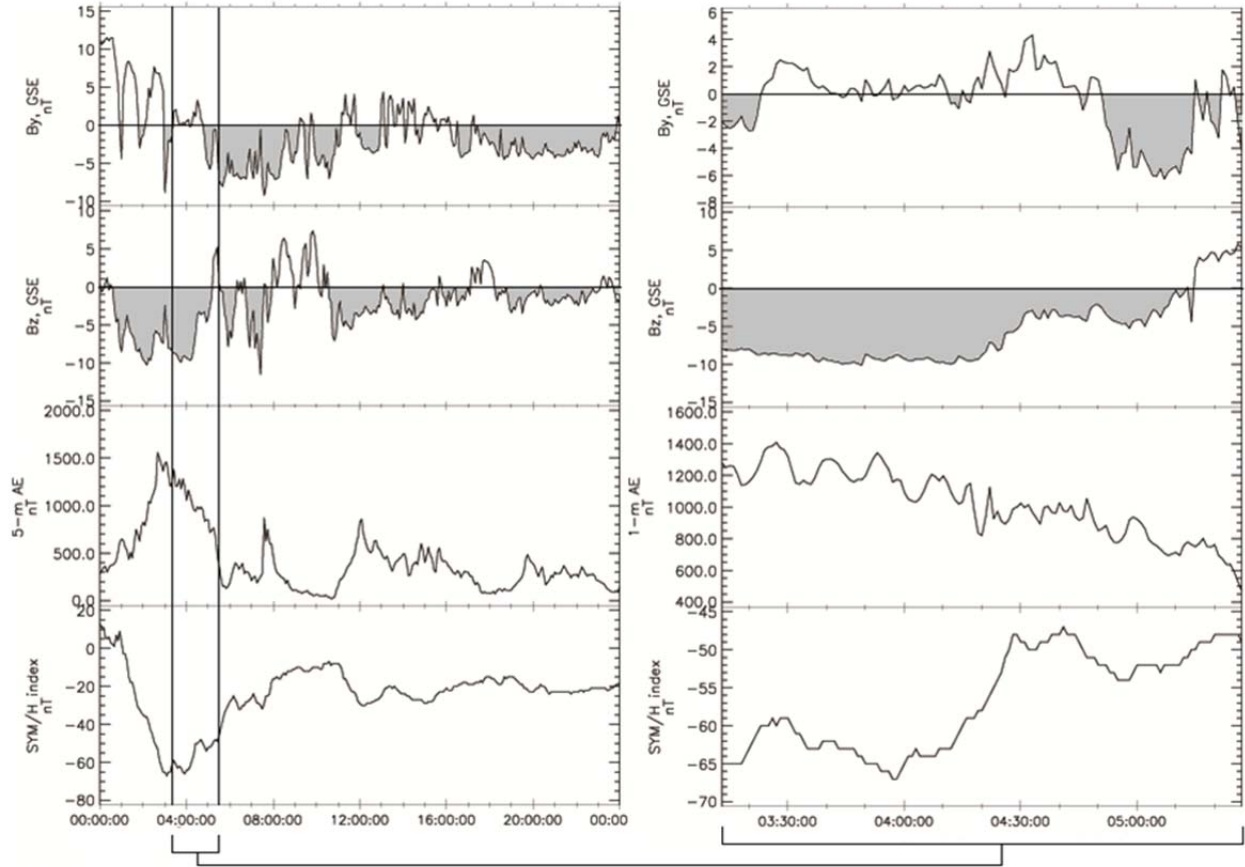
18

**Figure 15: The IMF By, Bz and AE, Sym-H indices for September 4, 2008 (left) and 0313 UT-0527 UT (right).**

The geomagnetic field measured by Geotail in the plasma sheet (x=~-17 $R_e$) is shown in Figure 16 (left). The ion number density and ion bulk flow velocity measured by the Solar Wind Analyzer (SWA) instrument are shown on the right of Figure 16. A bursty bulk flow (BBF) [*Angelopoulos et al*., 1994] is identified at 0418 UT by the large Earthward $V_x$ component of the ion bulk flow velocity and the positive turn in $B_z$. The large $B_x$ component of the geomagnetic field measured by Geotail prior to the injection shows the field stretching until the dipolarization is observed. Figure 17 shows the geomagnetic field at geosynchronous orbit measured by GOES-12 (left) and GOES-11 (right). The GOES spacecraft locations for this interval are shown in Figure 18. Both GOES spacecraft see the dipolarization just prior to 0430 UT.
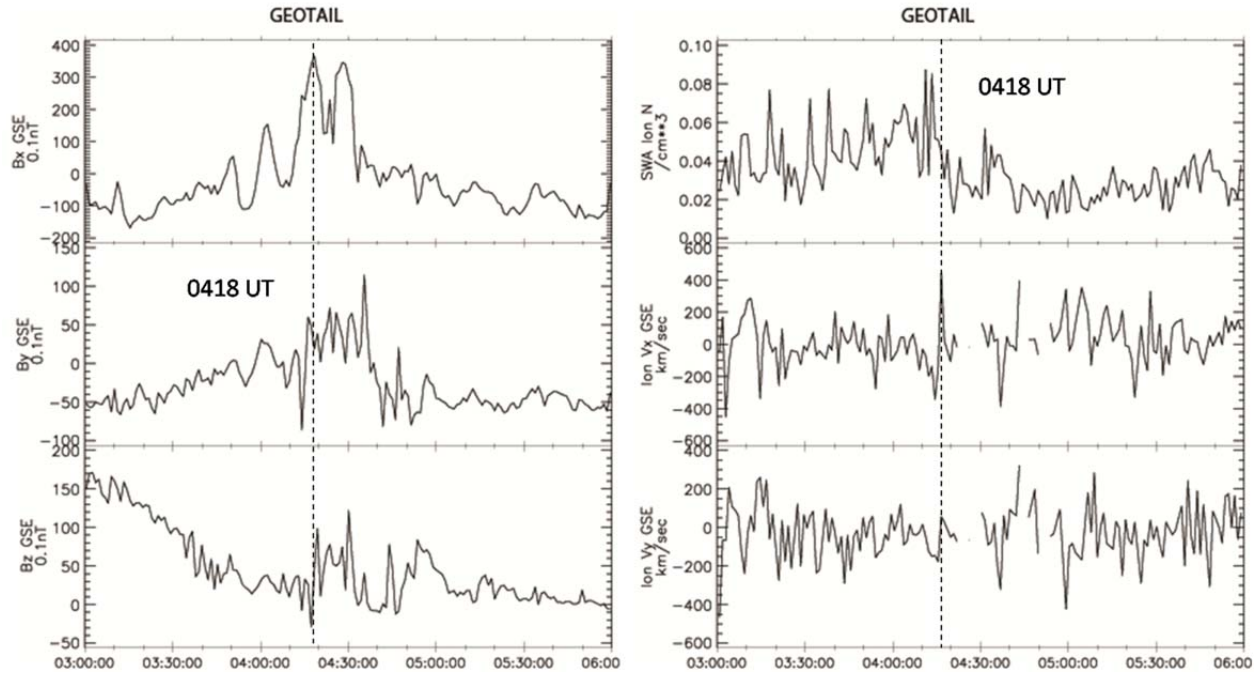
19

**Figure 16: Geotail geomagnetic field data (left) and ion density, $V_x$ and $V_y$ (right) for 0300 UT - 0600 UT on September 4, 2008. The dashed vertical line indicates the dipolarization and plasma injection at 0418 UT.**
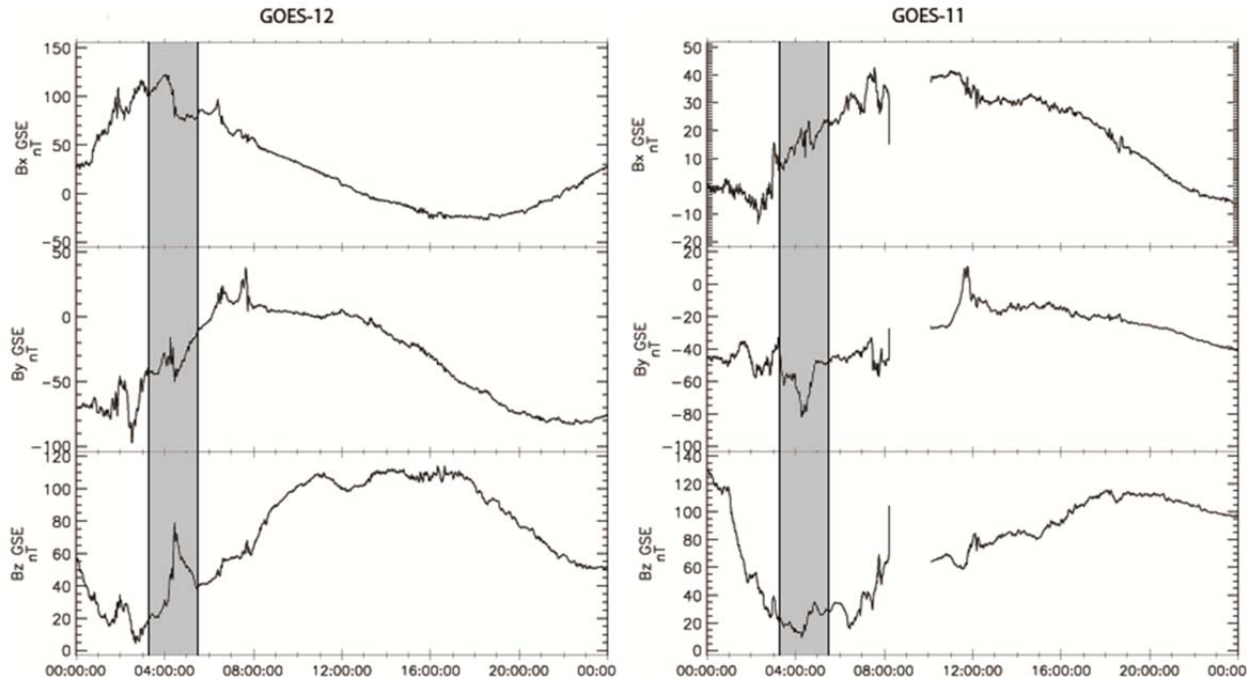


**Figure 17: GOES-12 (left) and GOES-11 (right) geomagnetic field data for September 4, 2008.**
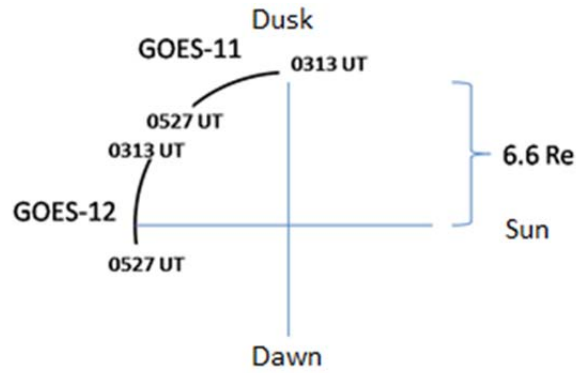
**Figure 18: GOES equatorial spacecraft locations for 0313 UT - 0527 UT on September 4, 2008.**

The 10 keV ENA images from TWINS-1 for 0313-0527 UT are shown in Figure 19. TWINS-1 is near apogee (R=7.12 $R_e$), viewing from dawn at the beginning of the observations. Low altitude emissions are clearly visible throughout the entire interval. They first peak during 0313-0346 UT, drop off during 0346 UT, come back during 0420-0454 UT and then drop off again. High altitude emissions from dawn to midnight are also visible at all times, and gradually increase from 0420-0454 UT to 0454-0527 UT.

As an example of the energy dependent global images during this period, the deconvolved equatorial ion intensities for 5-30 keV ions during 0347-0420 UT are shown in Figure 20. Prior to the plasma injection, a single peak is observed at midnight between L=3 and L=5 $R_e$.
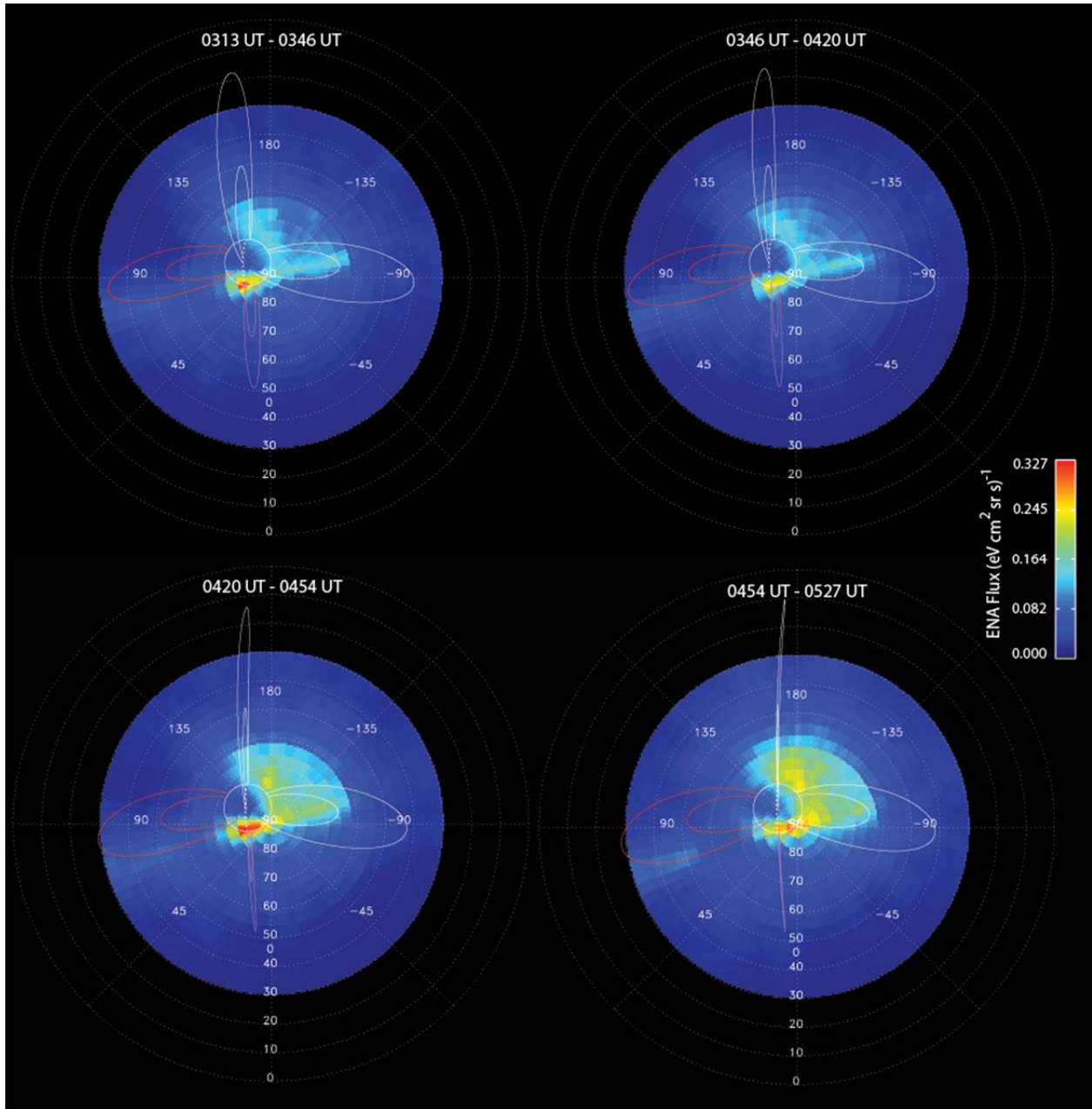
**Figure 19: TWINS-1 10 keV ENA flux for 0313–0527 UT on 4 September 2008.**
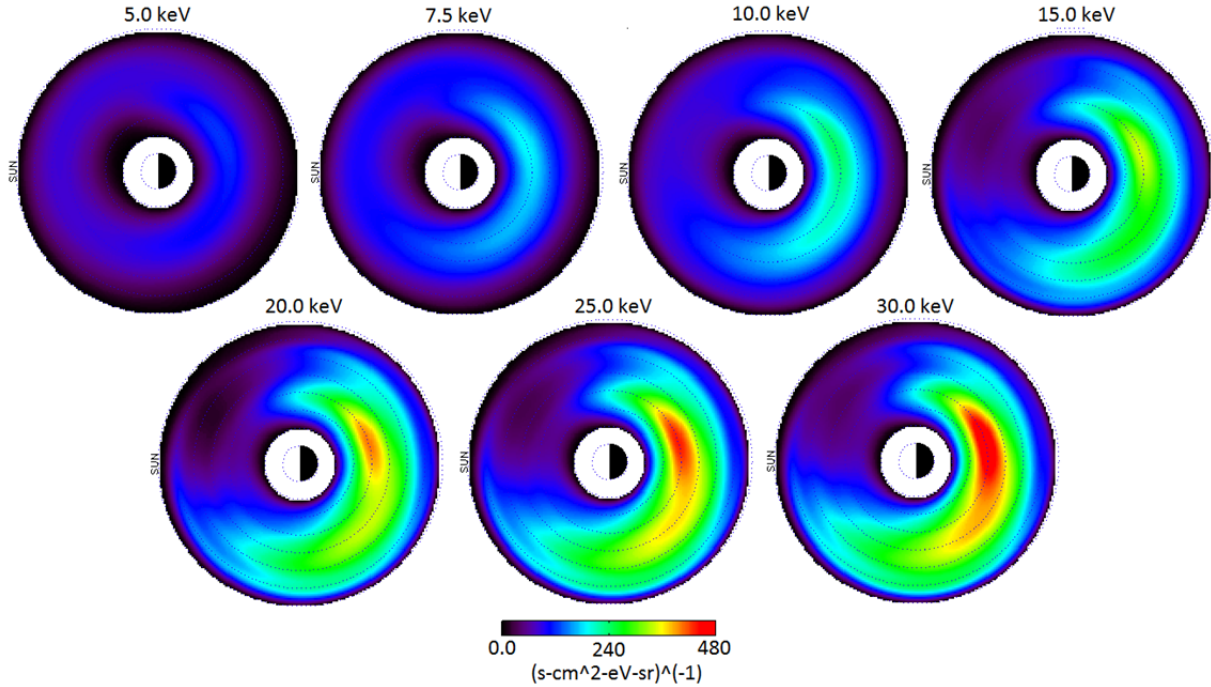
**Figure 20: Equatorial intensity averaged over pitch angle for 5-30 keV ions on September 4, 2008, 0347 UT - 0420 UT.**

Figure 21 shows the evolution of the energy spectrum in the peak at midnight throughout the entire time period (0313-0527 UT). The peak in ion intensity appears to be at an energy higher than 30.0 keV both prior to and after the injection. We compare the ENA intensity calculated from the result of the inversion to the measured ENA intensity for 0454-0527 UT in Figure 22 (10 keV) and Figure 23 (20 keV). The bright emissions from the outer pixels beneath the sun line in the measured intensity are due to instrumental effects and are not reproduced by the deconvolved ion intensity. The ENA intensity calculated from the ion distribution produces the same overall features as in the measured ENA intensity, indicating that the ion distribution the inversion technique produces well explain the measured ENA intensity.

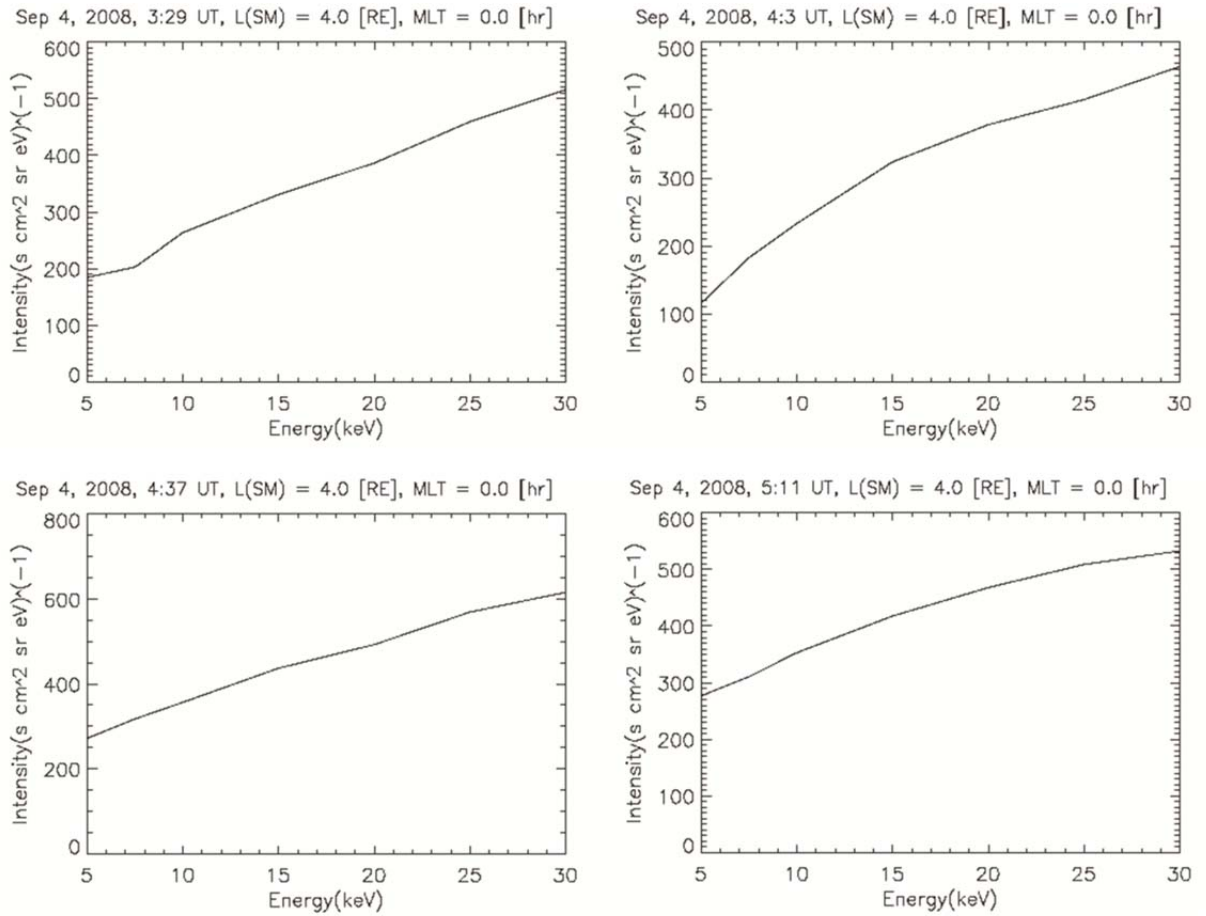**Figure 21: Evolution of 5-30 keV ion intensity spectra at L=4, MLT=0.0 on September 4, 2008, 0313 UT - 0527 UT.**
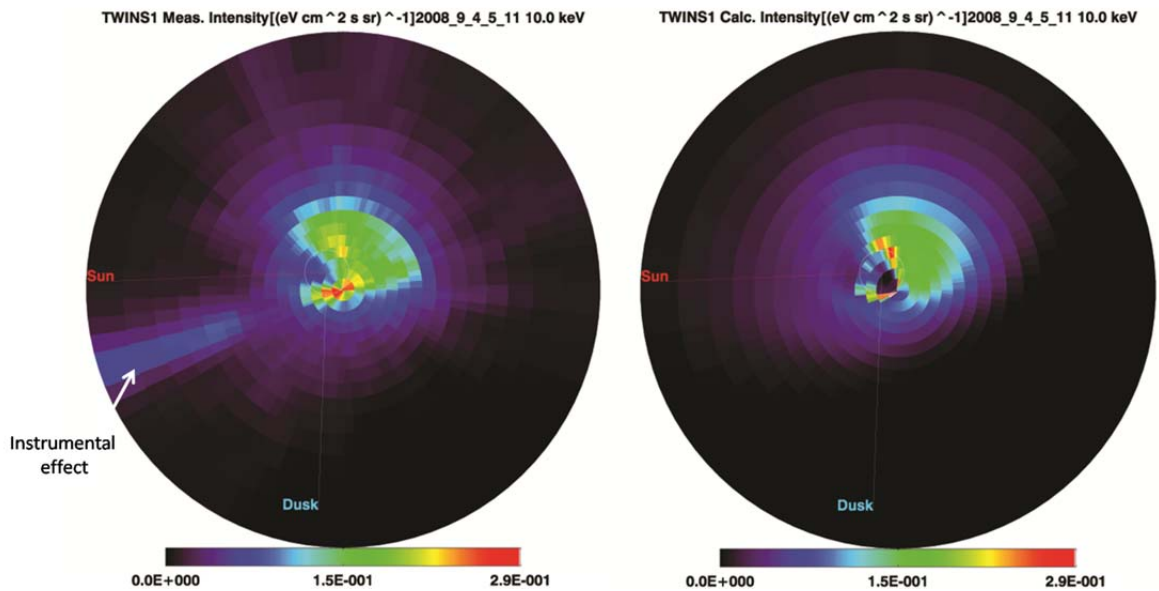


**Figure 22: 10 keV measured ENA intensity (left) and calculated ENA intensity (right) for 0454 - 0527 UT on September 4, 2008.**
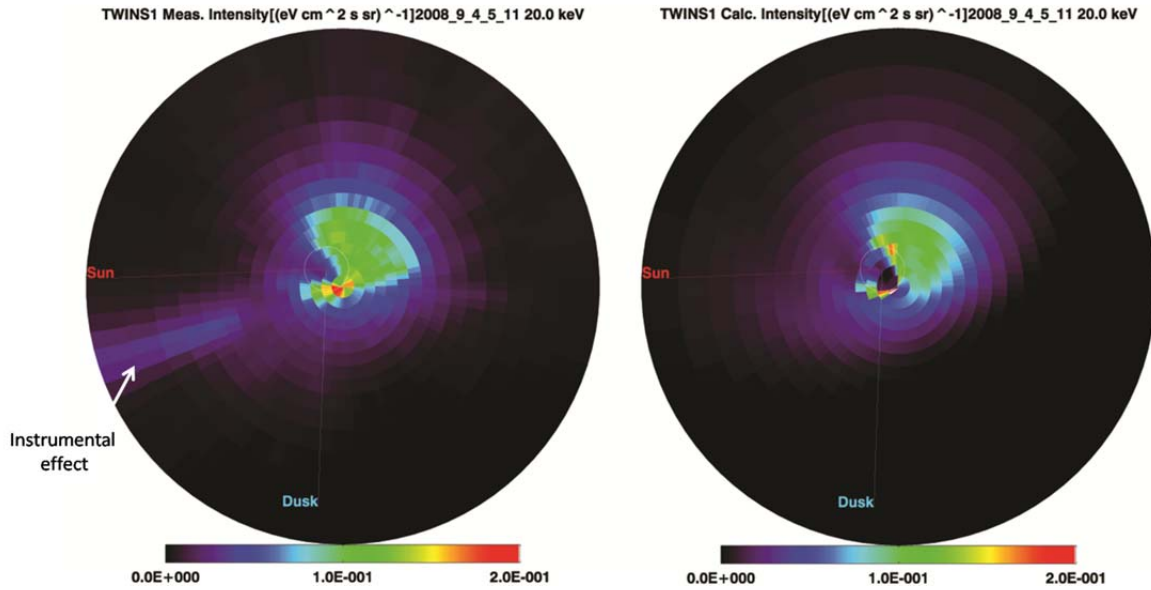
**Figure 23: 20 keV measured ENA intensity (left) and calculated ENA intensity (right) for 0454 - 0527 UT on September 4, 2008.**
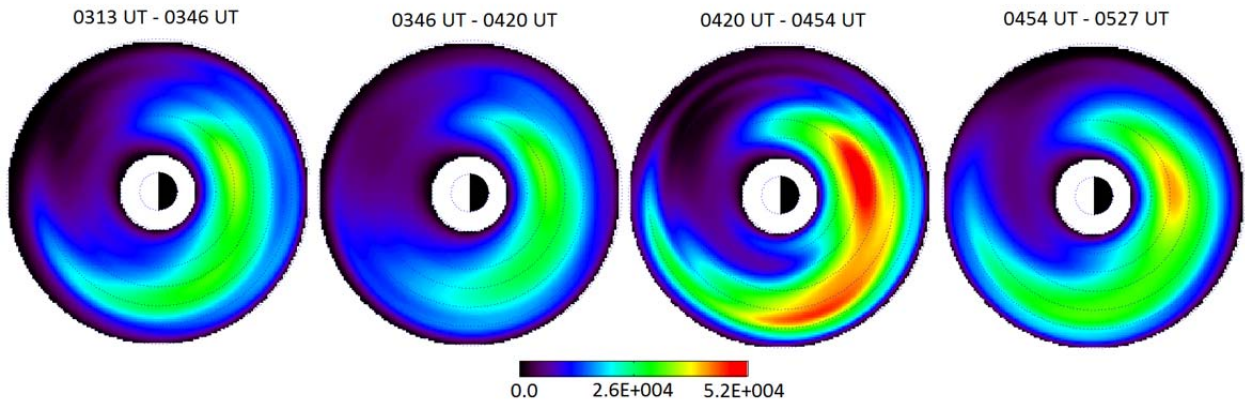


**Figure 24: 5-30keV equatorial energy density profiles for 0313 UT - 0527 UT on September 4, 2008.**

The equatorial energy densities calculated from the deconvolved ion distribution for the entire interval are shown in Figure 24. The energy density in the ring current peaks slightly duskward of midnight during 0313-0420 UT. It then increases in two locations, one between L=3 and L=5 $R_e$ which is still slightly in the post midnight region and one at L=6 $R_e$ with its peak reaching from dusk to midnight. The energy density in the ring current then drops off again

25

during 0454-0527 UT. The peak at midnight remains in the same location while the peak between dusk to midnight has disappeared. The strength of the energy density between 5 and 30 keV appears to be driven by an injection associated with a dipolarization observed at geosynchronous and deeper in the tail rather than following Sym-H.

**3. Geomagnetic Storms Driven by Interplanetary Coronal Mass Ejections (ICMEs)**

The geomagnetic storms presented in this section occurred during early 2011 and are due to interplanetary coronal mass ejections (ICMEs), also known as solar flares. The storm drivers were identified by a sharp increase in the 1-8 Angstrom and 0.5-4.0 Angstrom solar X-ray flux observed by the GOES spacecraft 1-2 days prior to the ICMEs reaching Earth. The storm drivers can further be identified by a prolonged negative excursion in IMF $B_z$ and the relatively quick storm recovery time [*Borovsky and Denton*, 2006]. Like to the CIR-driven storms in the previous section, the storms in this section are only small to moderate sized as defined by *Gonzalez et al*. [1994].

The 11 March 2011 Event

Figure 25 shows the 1-minute averages of the $B_y$ and $B_z$ components of the interplanetary magnetic field (IMF), as well as the auroral electrojet (AE), Sym-H (symmetric) and ASym-H (anti-symmetric) indices provided by OMNI for the days of March 10-12, 2011. In this section, we focus on the late main and early recovery phases of the storm identified by the thick vertical lines drawn during the first half (0100 UT to 1030 UT) of March 11, 2011. The $B_y$ component of the IMF is slightly positive during the first half and slightly negative during the latter half of the interval of interest, while IMF $B_z$ is negative throughout the entire interval. As with the previous section, the IMF conditions are time shifted to the magnetopause by OMNI. The AE index remains elevated throughout the interval and peaks slightly above 1000 nT in the late main phase of the storm. For the interval of interest, Sym-H begins at approximately -60 nT at 0100 UT and dips to nearly -90 nT just after 0500 UT. As with the CIR-driven storms, this negative excursion of Sym-H between 0100 UT and 0500 UT indicates the main phase of the storm. After

0500 UT, Sym-H begins to recover and nearly reaches -60 nT by the end of the interval at 1030 UT. The anti-symmetric component (as observed through the ASym-H index) of the ring current remains elevated throughout the interval and peaks just slightly before the end of the main phase between 0400 UT and 0500 UT.
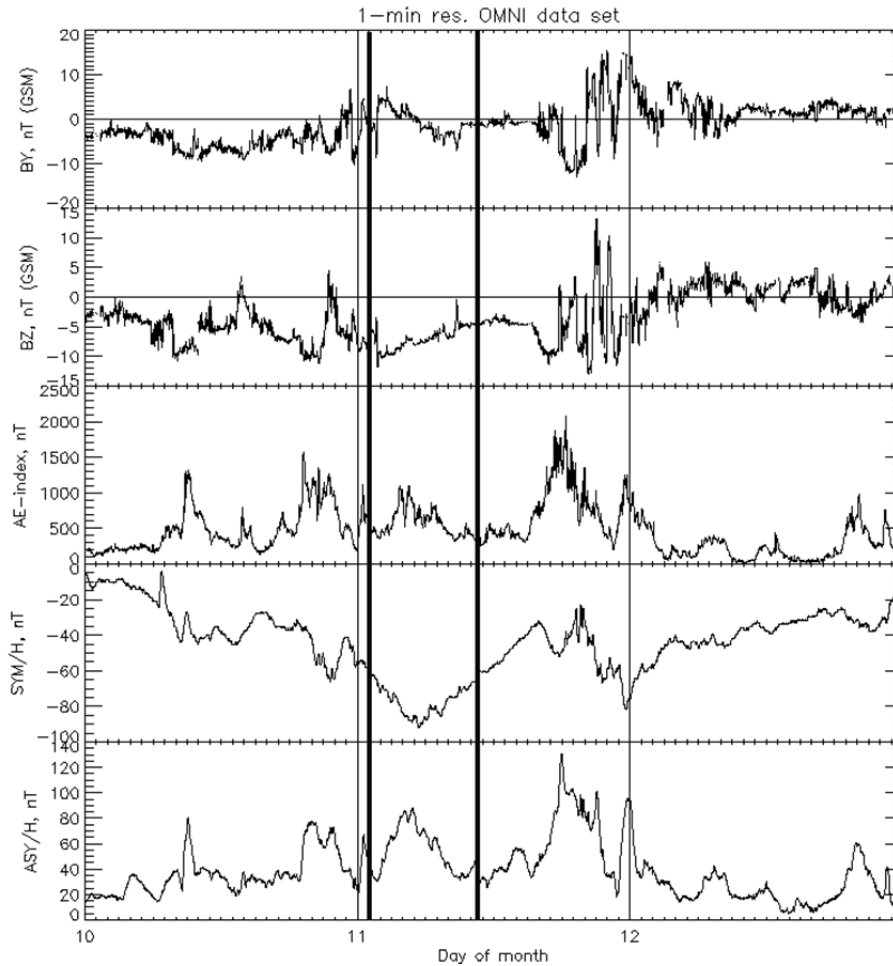


**Figure 25: The IMF B$_y$, B$_z$ and AE, Sym-H, Asym-H indices for March 10-12, 2011.**

Figure 26 shows the 15 keV energetic neutral atom (ENA) flux observed by TWINS-2 between 0100 UT and 0430 UT and TWINS-1 between 0500 UT and 1030 UT. Note that, unlike the previous section, here we chose to use data for the first 30 minute interval of each hour so as to cover a larger portion of the storm; the ENA images for the latter 30 minutes of each hour are

very similar to the first 30 minutes. The ENA images in this section are 25 sweep, approximately 30 minute averages. The slight difference in integration time between this section and the previous section are due to a change in the amount of time used in buffering between sweeps made to the instruments in July, 2009. Like the ENA images in the previous section, dipole field lines are drawn at L=4 and L=8 $R_e$, with the red and purple field lines indicating the sunward and duskward directions, respectfully. The TWINS-2 spacecraft is located on the dayside at R=7 $R_e$, 55.6 degrees latitude at an MLT of approximately 10. Over the course of the interval 0100 UT – 0430 UT, TWINS-2 moves towards dusk, eventually ending its observations at R=6 $R_e$, 49 degrees latitude and 13.5 MLT. TWINS-1 begins its observations at 0500 UT on the dawnside (5.2 MLT), at R=5.8 $R_e$, 58.6 degrees latitude. After going through apogee, TWINS-1 and ends its observations at 1030 UT, close to noon (11 MLT) at R=6.3 $R_e$, 59 degrees latitude. The maximum on the color bar for all images is set to the maximum for the entire interval, which occurs during 0400-0430 UT in TWINS-2. As with the previous section, the maximum occurs in pixels attributed to low altitude emissions (LAEs) just off Earth's limb.
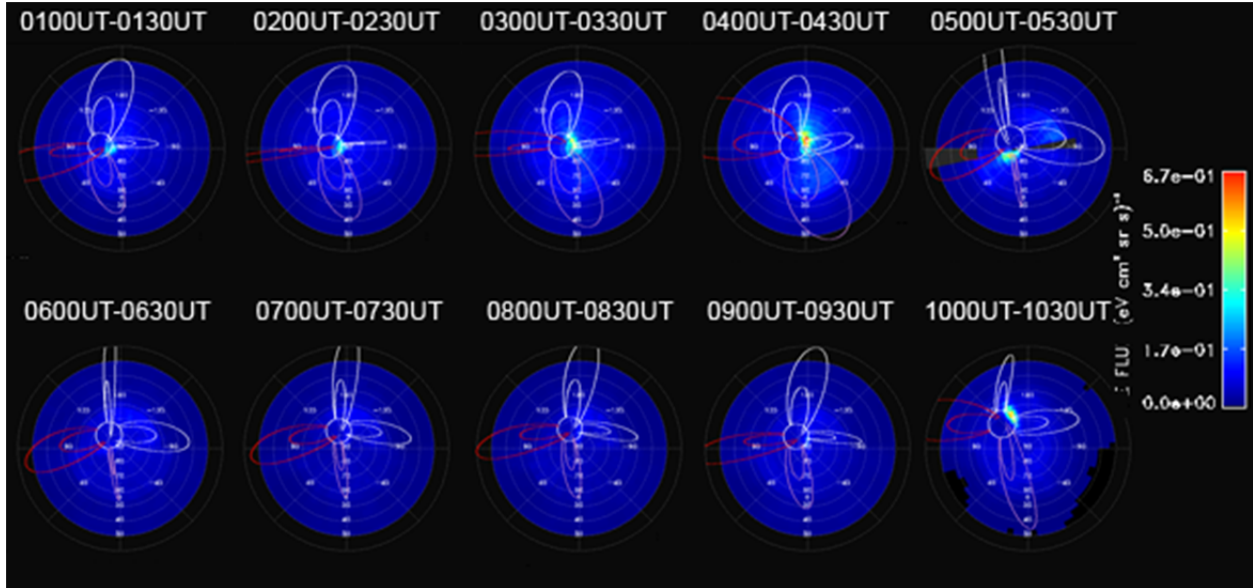
**Figure 26: TWINS-2 15 keV ENA flux for 0100-0430UT and TWINS-1 15 keV ENA flux for 0500UT-1030UT on 11 March 2011.**

The deconvolved 5-65 keV equatorial energy density profiles for 0100 UT to 1030 UT on March 11, 2011 is presented in Figure 27. The peak in energy density is found to be in the midnight region between L=5 – 7 $R_e$. Despite the peak in ENA intensity being at 0400 UT - 0430 UT, the peak in the deconvolved energy density is found to be at 0330 UT – 0400 UT. This difference in the timing can be explained by the fact that the ENA intensity is taken at a single energy (15 keV) and the energy density is integrated over a much more broad energy range (5-65 keV). The energy density remains anti-symmetric throughout the entire interval, moving slightly into the pre-midnight region after minimum Sym-H.
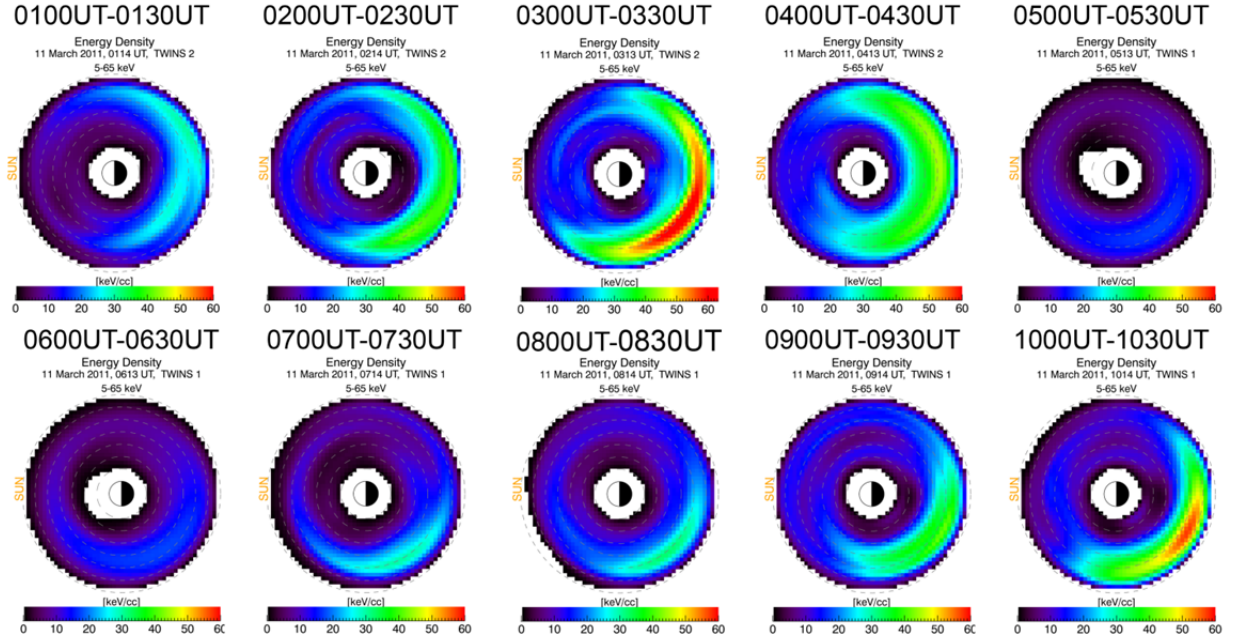
**Figure 27: 5-65 keV equatorial energy density profiles for (a) TWINS-2 at 0100UT-0430UT and (b) TWINS-1 at 0500-1030UT on March 11, 2011.**

The equatorial pitch angle anisotropy for March 11, 2011, taken at 15 keV, is shown in Figure 28. To calculate the pitch angle anisotropy, we adopt the method similar to that used by *Chen et al* [1998],

$$A = \frac{I_\perp - 2I_\parallel}{I_\perp + 2I_\parallel}$$

$$I_\perp = \int_{-1}^{1} f_{eq} \sin^2 \psi \, d(\cos \psi)$$

$$I_\parallel = \int_{-1}^{1} f_{eq} \cos^2 \psi \, d(\cos \psi)$$

Using this definition, -1 represents a field aligned pitch angle distribution and +1 represents a perpendicular distribution. From Figure 28, the pitch angle distribution is isotropic and nearly uniform in the equatorial plane throughout the interval, with the exception of L=5.5 to L=8 $R_e$ on the night side from 0100 UT to 0830 UT; in this region, the pitch angle distribution is

much more field aligned. It is important to note that this region is also where the peak in the distribution is observed in Figure 27.
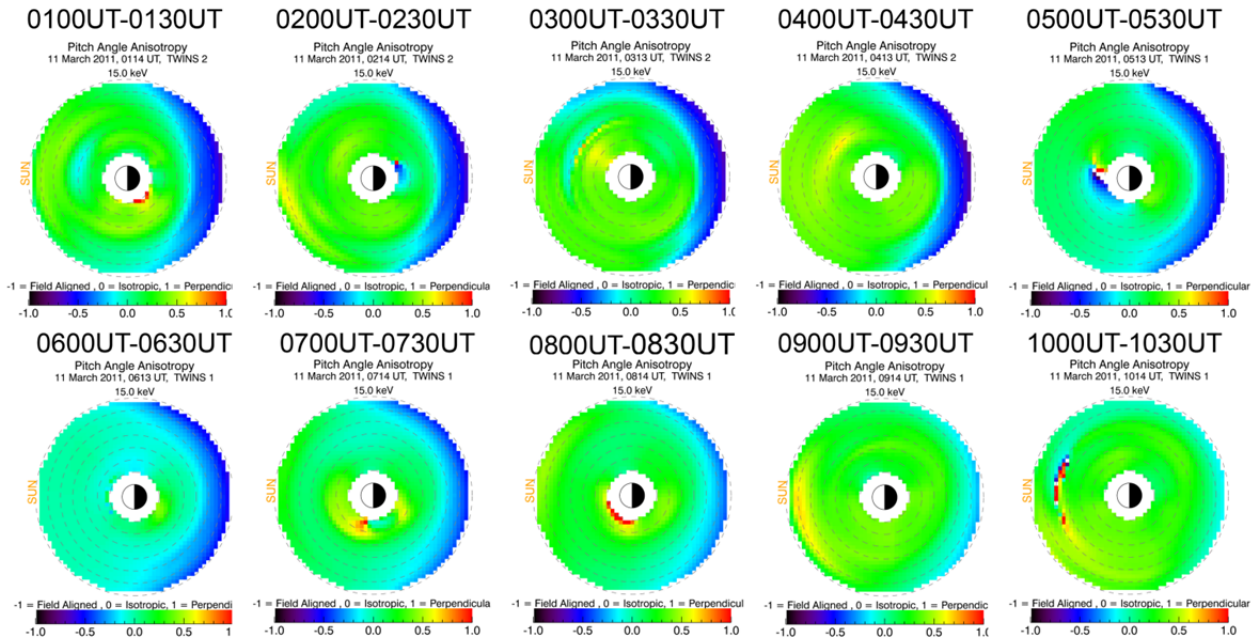


**Figure 28: Pitch angle anisotropy at 15 keV for (a) TWINS-2 at 0100UT-0430UT and (b) TWINS-1 at 0500-1030UT on March 11, 2011.**


The 28 May 2011 Event

Figure 29 shows the 1-minute averages of the $B_y$ and $B_z$ components of the IMF, as well as the auroral electrojet (AE), Sym-H (symmetric) and ASym-H (anti-symmetric) indices provided by OMNI for the days of May 27-29, 2011. In this section, we focus on the early recovery phase of the storm, again identified by the thick vertical lines during the middle of the day (1100 UT to 1530UT) on May 28, 2011. The IMF $B_y$ is strongly negative throughout the entire interval, reaching approximately -10 nT around 1400 UT. The $B_z$ component of the IMF begins the interval strongly negative, but goes positive around 1330 UT. As with before, these interplanetary conditions are time shifted to the magnetopause by OMNI. The AE index begins

the interval elevated and peaks above 1000 nT just before 1300 UT, then quickly drops towards

the end of the interval.  It should be noted that the timing of the drop in AE towards the end of

the interval is correlated to the positive excursion of the $B_z$ component of the IMF towards the

end of the interval.  The Sym-H index reaches a minimum of approximately -85 nT at 1200 UT,

then quickly jumps nearly 20nT to -60 nT by 1300 UT. The ASym-H index is elevated

throughout the interval, again indicating an anti-symmetric ring current configuration. It should

be noted that while it is elevated throughout the entire interval, the ASym-H index varies greatly,

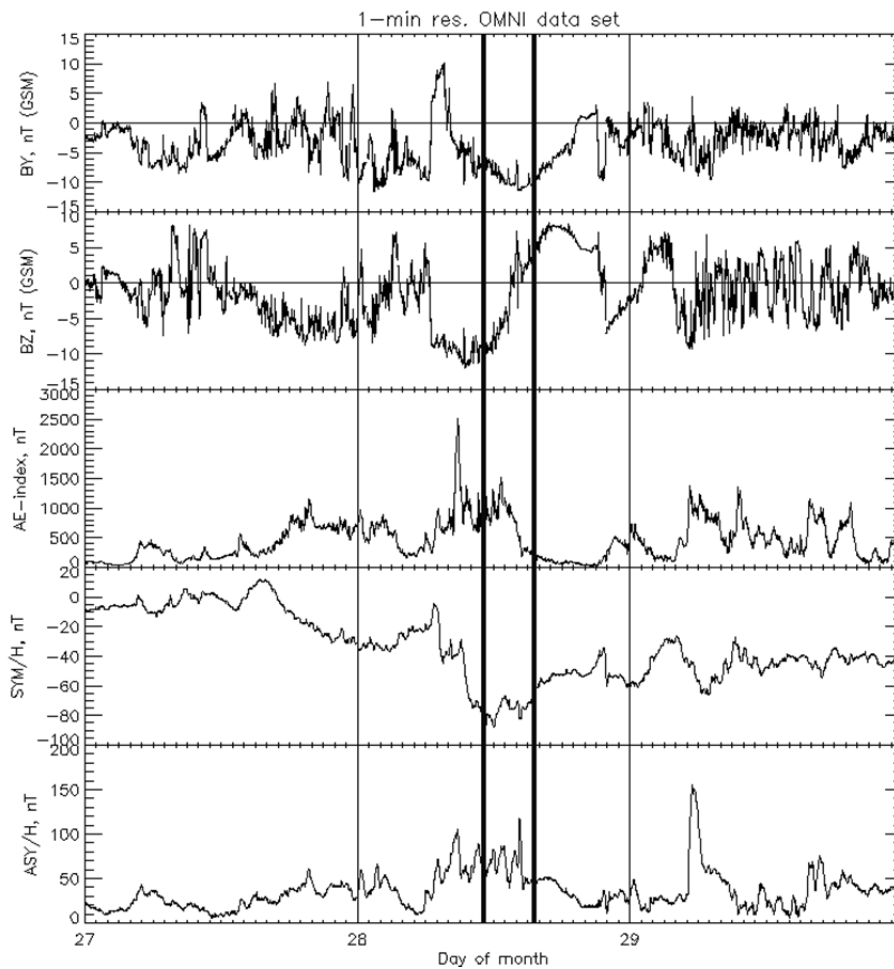jumping and dropping approximately 50 nT in around an hour at 1400 UT.



**Figure 29: The IMF $B_y$, $B_z$ and AE, Sym-H, Asym-H indices for May 27-29, 2011.**
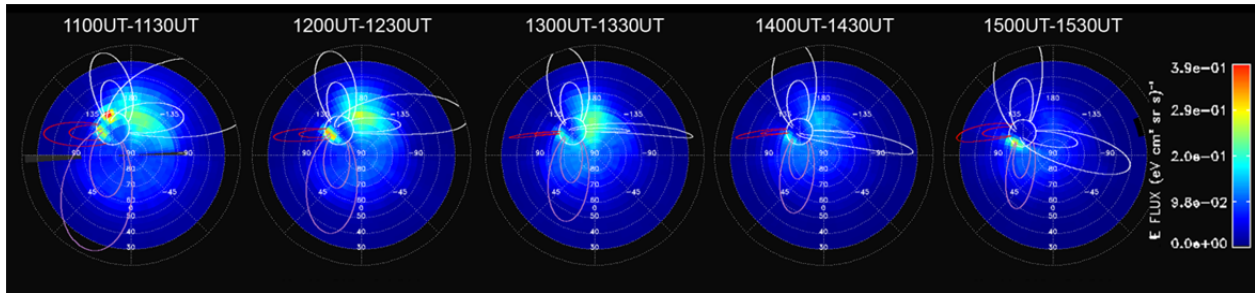
**Figure 30: TWINS-1 15 keV ENA flux for 1100-1530UT on 28 May 2011.**

The 15 keV TWINS-1 ENA intensities for 1100 UT – 1530 UT on May 28, 2011 are shown in Figure 30. As with the March 11, 2011 case, we only show the first 30 minutes (again, 25 sweeps) of each hour so as to cover a larger portion of the storm. Also, as with the previous cases, the purple and red L-shells indicate the duskward and sunward directions. At 1100 UT, TWINS-1 is at R=5.5 Re, 47 degrees latitude and is observing ENAs from the pre-midnight region (~21.5 MLT). The spacecraft goes through apogee around 1400 UT and is eventually in the post-midnight region (MLT=2) at R=6.8 Re, 57 degrees latitude at 1500 UT. The peak in ENA intensity is observed in the LAEs during the 1100 UT – 1130 UT interval, then drops to less than half its peak value at 1400 UT – 1430 UT. The ENA intensity then jumps slightly during the 1500 UT – 1530 UT interval. Unlike the previous (March 11) case, there are considerable high altitude emissions observed in addition to the low altitude emissions.
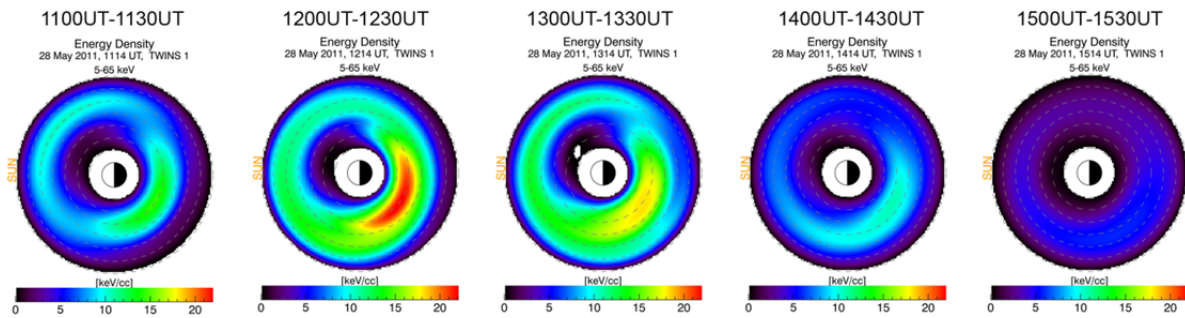


**Figure 31: 5-65keV equatorial energy density profiles for TWINS-1 at 1100UT-1530UT on May 28, 2011.**

The deconvolved 5-65 keV equatorial energy density for 1100 UT – 1530 UT on May 28, 2011 is shown in Figure 31. Throughout the observation period, the peak in energy density is found to be between L=3 and L=5 $R_e$ on the night side.  The peak, approximately 22 keV/cc, occurs during the 1200 UT - 1230 UT interval (again, correlated with the ~1000 nT peak in the AE index). As with the March 11, 2011 case, the peak in energy density is does not occur during the same interval as the peak in ENA intensity; we can again explain this by the fact that energy density is integrated over 5-65 keV, while the ENA intensity is taken at 15 keV. It should be noted that the energy density is much more symmetric during the 1100 UT – 1330 UT interval than the 1400 UT – 1530 UT interval. The timing of the change in symmetry correlates with the 50 nT jump in the ASym-H index seen in Figure 29.
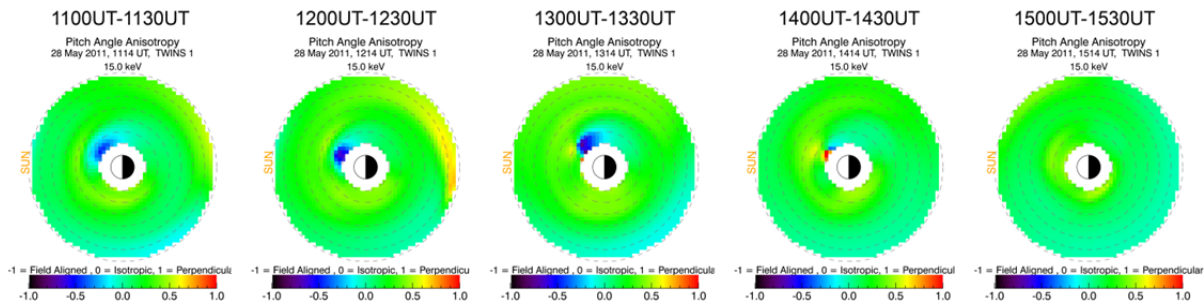


**Figure 32: Pitch angle anisotropy at 15 keV for TWINS-1 at 1100UT-1530UT on May 28, 2011.**

Figure 32 shows the TWINS-1 pitch angle anisotropy at 15 keV for 1100 UT – 1530 UT on May 28, 2011.  As with the previous case, the equatorial distribution is nearly isotropic and uniform in the equatorial plane. The slight perpendicular distribution near L=7 Re during the 1200 UT – 1230 UT interval is likely the result of low data in that region (see Figure 31).  Unlike the previous (March 11, 2011) case, the peak in the distribution is nearly isotropic.

## 4. Discussion

One important aspect of analyzing the ENA images presented in this thesis is in understanding the impact of geocoronal density at different altitudes. Due to the higher geocoronal density at low altitudes, precipitating particles tend to dominate the ENA emissions. These low altitude emissions typically belong to a ring current plasma population on the opposite side of Earth, and are viewed just off Earth's limb [*Roelof*, 1987; *Bazell et al.*, 2010]. These emissions are clear in Figures 2, 9, 19, 26 and 30. It should be noted that the link between sources in the ring current intensity and the low altitude emissions depends upon the use of the thick target approximation, as described by *Bazell et al.* [2010], and the magnetic field mapping.

The higher energy density in the pre-midnight sector shown in Figure 7 is believed to be the source of the precipitating particles creating the low altitude emissions seen off the Earth's limb in Figure 2. Note that the low altitude emissions are observed from both hemispheres throughout 0330-0511 UT. The low altitude emissions in Figure 9 are also clearly observed just off the Earth's limb. These are believed to originate from the duskward peak in ring current energy density in Figure 14. We observe low altitude emissions emanating from both hemispheres again for the September 4 storm in Figure 19. Again, these are believed to have their sources in the duskward peak in energy density in Figure 24. In Figure 30, the low altitude emissions are again observed from both hemispheres for 1100 UT to 1430 UT. It is extremely interesting to note that the LAEs emanating from the southern hemisphere for the May 2011 event disappear toward the end of the interval of interest. This corresponds to a less symmetric

ring current observed during these later times (1400 UT to 1530 UT) in Figure 31. For each CIR-driven storm, ENA intensity increases after the dipolarization signature is seen at geosynchronous. For the ICME-driven storms, ENA intensity increases after substorms are inferred from increases in AE index. These observations, i.e., ENA intensity following substorm activity, are consistent with previous observations by *Lui et al.* [2001] and *Ohtani et al.* [2005].

As with the CIR-driven storms, the peak in energy density in the ICME-driven storms seen in Figure 27 is believed to be due to the low altitude emissions observed in Figure 26. Due to the viewing geometry in this case (March 2011), the observed plasma is field aligned. This is confirmed by the pitch angle anisotropy in Figure 28, where the peak in energy density from Figure 27 is more field aligned during 0100 UT to 0730 UT. It is important to note that this is thought to be primarily due to viewing geometry of the spacecraft, which is observing the night side distribution primarily through the LAEs just off the Earth's limb; that is, there may be a more isotropic or more perpendicular distribution which cannot be seen by the spacecraft at this location.

Due to the lack of availability of high resolution GOES magnetometer data at geosynchronous orbit during the ICME-driven storms in 2011, confirming depolarization signatures during these storms is more difficult. Nevertheless, substorm activity can still be inferred by peaks in the AE index [*Newell and Gjerloev*, 2011]. Dipolarization signatures are observed near minimum Sym-H for the August 2008, September 2008, March 2011 and May 2011 events, which is consistent with previous geosynchronous observations [*Iyemori and Rao*, 1996; *Ohtani et al.,* 2001]. The immediate increase in Sym-H following the substorm injection is believed to be due to a reduction of the cross tail current [*Siscoe and Petscheck*, 1997]. We find that just after a plasma injection during CIR-driven storms, there are often two peaks in the 5-30

keV ring current plasma energy density, one near midnight between L=3 and L=5, and one between dusk and midnight between L=5 and L=7. During the ICME-driven storms, only one peak is observed in the plasma energy density. The peak in 5-65 keV energy density tends to be located primarily in the pre-midnight region, which is consistent with the in-situ observations of the ring current shown by *Le et al.* [2004] and *Lui* [2003], as well as the in-situ geosynchronous MPA observations [*Korth et al.*, 1999; *Denton et al.*, 2005; *Zhang et al.*, 2006] and simulations of plasma pressure in the ring current [*Zhang et al.*, 2007].

To summarize, we have shown global images of trapped ring current particles with energies between 5 and 65 keV during the main phase and early-recovery phase of CIR and ICME-driven storms. For the CIR-driven storms, we also have shown the energy spectra as a function of time. Of particular interest is the fact that during the early recovery phase of the strongest CIR-driven storm, where Sym-H dips below -65 nT and AE is greater than 1000 nT, the peak of the ion intensity in the ring current is greater than 30 keV. On the other hand, during the main and early recovery phases of the smaller storms, the peak of the ion intensity is around 10-15 keV. For the ICME-driven storms, we have shown the pitch angle distribution is nearly isotropic and uniform in the equatorial plane; the one exception to this is the peak in plasma energy density during the March 11, 2011 event, where a more field aligned distribution is observed. This anisotropy is thought to be due to spacecraft viewing geometry. These relationships between the storm conditions (both interplanetary and magnetospheric) and the ring current energy density do not appear to be casual, and detailed modeling analysis is needed to further understand the specifics of the spatial distribution and the energy spectra in context of the storm conditions. However, all five events used in this study show that the energy density of 5-

65 keV ions in the ring current does not follow Sym-H, but rather is directly and significantly enhanced by injections during both the main and early recovery phases of geomagnetic storms.

## References

Angelopoulos, V., C. Kennel, F. Coroniti, R. Pellat, M. Kivelson, R. Walker, C. Russell, W. Baumjohann, W. Feldman, and J. Gosling (1994), Statistical Characteristics of Bursty Bulk Flow Events, J. Geophys. Res., 99(A11), 21257-21280.

Barnett, C. F. (1990), Atomic Data for Fusion, Volume 1: Collisions of H, H2, He, and Li Atoms and Ions with Atoms and Molecules, Technical Report ORNL-6086/V1, Oak Ridge National Laboratory, Oak Ridge, TN 37831

Bazell, D., E. C. Roelof, T. Sotirelis, P. C. Brandt, H. Nair, P. Valek, J. Goldstein, D. McComas (2010), Comparison of TWINS Images of Low-Altitude 1 Emission of Energetic Neutral Atoms with DMSP 2 Precipitating Ion Fluxes, J. Geophys. Res., Submitted.

Borovsky, J. E., and M. H. Denton (2006), Differences between CME-driven storms and CIR-driven storms, J. Geophys. Res., 111, A07S08, doi:10.1029/2005JA011447.

Brandt, P. C., S. Ohtani, D. G. Mitchell, M.-C. Fok, E. C. Roelof, and R. Demajistre (2002), Global ENA observations of the storm mainphase ring current: Implications for skewed electric fields in the inner magnetosphere, Geophys. Res. Lett., 29 (20), 1359, doi:10.1029/2002GL015160.

Buzulukova, N., M.-C. Fok, J. Goldstein, P. Valek, D. J. McComas, P. C. Brandt (2010), Ring current dynamics in modest and strong storms: comparative analysis of TWINS and IMAGE/HENA data with CRCM, J. Geophys. Res., submitted.

Chen, M. W., J. L. Roeder, J. F. Fennell, L. R. Lyons, and M. Schulz (1998), Simulations of ring current proton pitch angle distributions, J. Geophys. Res., 103(A1), 165–178, doi:10.1029/97JA02633.

deBoor, Carl (1978), A Practical Guide to Splines, Springer-Verlag, N.Y.

Denton, M. H., M. F. Thomsen, H. Korth, S. Lynch, J. C. Zhang, and M. W. Liemohn (2005), Bulk plasma properties at geosynchronous orbit, J. Geophys. Res., 110, A07223, doi:10.1029/2004JA010861.

Denton, M. H., J. E. Borovsky, R. M. Skoug, M. F. Thomsen, B. Lavraud, M. G. Henderson, R. L. McPherron, J. C. Zhang, and M. W. Liemohn (2006), Geomagnetic storms driven by ICME- and CIR-dominated solar wind, J. Geophys. Res., 111, A07S07, doi:10.1029/2005JA011436.

Ebihara, Y., and M.-C. Fok (2004), Postmidnight storm-time enhancement of tens-of-keV proton flux, J. Geophys. Res., 109, 12,209, doi:10.1029/2004JA010523.

Ejiri, M., R. A. Hoffman, and P. H. Smith (1980), Energetic particle penetrations into the inner magnetosphere, J. Geophys. Res., 85(A2), 653–663.

Fok, M.-C., T. E. Moore, and M. E. Greenspan (1996), Ring current development during storm main phase, J. Geophys. Res., 101(A7), 15,311–15,322, doi:10.1029/96JA01274.

Gonzalez, W. D., J. A. Joselyn, Y. Kamide, H. W. Kroehl, G. Rostoker, B. T. Tsurutani, and V. M. Vasyliunas (1994), What is a Geomagnetic Storm?, J. Geophys. Res., 99(A4), 5771–5792, doi:10.1029/93JA02867.

Iyemori, T., and D. R. K. Rao (1996), Decay of the Dst field of geomagnetic disturbances after substorm onset and its implication to substorm relation, Ann. Geophys., 14, 608.

Kistler, L. M., and D. J. Larson (2000), Testing electric and magnetic field models of the storm-time inner magnetosphere, J. Geophys. Res., 105(A11), 25,221–25,231, doi:10.1029/2000JA000132.

Korth, H., M. F. Thomsen, J. E. Borovsky, and D. J. McComas (1999), Plasma sheet access to geosynchronous orbit, J. Geophys. Res., 104(A11), 25,047–25,061, doi:10.1029/1999JA900292.

Krieger, A. S., A. F. Timothy, and E. C. Roelof (1973), A coronal hole and its identification as the source of a high velocity solar wind stream, Sol. Phys., 23, 123.

Le, G., C. Russell, and K. Takahashi (2004), Morphology of the ring current derived from magnetic field observations, Ann. Geophys., 22, 1267–1295.

Lui, A. T. Y., R. W. McEntire, M. Nosé, and D. J. Williams (2001), Composition of energetic neutral atoms during a storm main phase, Geophys. Res. Lett., 28(7), 1363–1366, doi:10.1029/2000GL012612.

Lui, A. T. Y. (2003), Inner magnetospheric plasma pressure distribution and its local time asymmetry, Geophys. Res. Lett., 30 (16), doi:10.1029/2003GL017596.

McComas, D. J. , F. Allegrini, J. Baldonado, B. Blake, P. C. Brandt, J. Burch, J. Clemmons, W. Crain, D. Delapp, R. DeMajistre, D. Everett, H. Fahr, L. Friesen, H. Funsten, J. Goldstein, M. Gruntman, R. Harbaugh, R. Harper, H. Henkel, C. Holmlund, G. Lay, D. Mabry, D. Mitchell, U. Nass, C. Pollock, S. Pope, M. Reno, S. Ritzau, E. Roelof, E. Scime, M. Sivjee, R. Skoug, T. S. Sotirelis, M. Thomsen, C. Urdiales, P. Valek, K. Viherkanto, S. Weidner, T. Ylikorpi, M. Young, J. Zoennchen (2009a), The Two Wide-angle Imaging Neutral-atom Spectrometers (TWINS) NASA Mission-of-Opportunity, Space Sci. Rev. 142, 157–231 DOI:10.1007/s11214-008-9467-4

McComas, D.J., F. Allegrini, P. Bochsler, M. Bzowski, E.R. Christian, G.B. Crew, R. DeMajistre, H. Fahr, H. Fichtner, P. Frisch, H.O. Funsten, S. A. Fuselier, G. Gloeckler, M. Gruntman, J. Heerikhuisen, V. Izmodenov, P. Janzen, P. Knappenberger, S. Krimigis, H. Kucharek, M. Lee, G. Livadiotis, S. Livi, R.J. MacDowall, D. Mitchell, E. Möbius, T. Moore,

N.V. Pogorelov, D. Reisenfeld, E. Roelof, L. Saul, N.A. Schwadron, P.W. Valek, R. Vanderspek, P. Wurz, and G.P. Zank (2009b), Global observations of the interstellar interaction from the Interstellar Boundary Explorer (IBEX), Science, 326, 959-962, doi: 10.1126/science.1180906.

McComas, D. J., N. Buzulukova, M. G. Connors, M. A. Dayeh, J. Goldstein, H. O. Funsten, S. Fuselier, N. A. Schwadron, and P. Valek (2012), Two Wide-Angle Imaging Neutral-Atom Spectrometers and Interstellar Boundary Explorer energetic neutral atom imaging of the 5 April 2010 substorm, J. Geophys. Res., 117, A03225, doi:10.1029/2011JA017273.

Newell, P. T., and J. W. Gjerloev (2011), Evaluation of SuperMAG auroral electrojet indices as indicators of substorms and auroral power, J. Geophys. Res., 116, A12211, doi:10.1029/2011JA016779.

Ohtani, S., M. Nosé, G. Rostoker, H. Singer, A. T. Y. Lui, and M. Nakamura (2001), Storm-substorm relationship: Contribution of the tail current to Dst, J. Geophys. Res., 106, 21,199–21,209, doi:10.1029/2000JA000400.

Ohtani, S., P. C. Brandt, D. G. Mitchell, H. Singer, M. Nosé, G. D. Reeves, and S. B. Mende (2005), Storm-substorm relationship: Variations of the hydrogen and oxygen energetic neutral atom intensities during storm-time substorms, J. Geophys. Res., 110, A07219, doi:10.1029/2004JA010954.

Østgaard, N., S. B. Mende, H. U. Frey, G. R. Gladstone, and H. Lauche (2003), Neutral hydrogen density profiles derived from geocoronal imaging, J. Geophys. Res., 108, A7, doi:10.1029/2002JA009749.

Perez, J. D. and G. Kozlowski and P. C. Brandt and D. G. Mitchell and J. M. Jahn and C. J. Pollock (2001), Initial ion equatorial pitch angle distributions from energetic netural atom images obtained by IMAGE, Geophys. Res. Lett., 28, 1155.

Perez, J. D., E. W. Grimes, J. Goldstein, D. J. McComas, P. Valek and N. Billor (2012), Evolution of CIR Storm on 22 July 2009, J. Geophys. Res., 2012JA017572

Roelof, E. C. (1987), Energetic neutral atom image of a storm-time ring current, Geophys. Res. Lett., 14(6), 652–655, doi:10.1029/GL014i006p00652.

Sandanger, M. I., F. Soraas, K. Aarsnes, K. Oksavik, D. S. Evans, and M. S. Greer (2005), Proton injections into the ring current associated with Bz variations during HILDCAA events, in The Inner Magnetosphere: Physics and Modeling, Geophys. Monogr. Ser., vol. 155, edited by T. I. Pulkkinen, N. A. Tsygenenko, and R. H. W. Friedel, p. 2249, AGU, Washington, D. C.

Siscoe, G. L., and H. E. Petschek (1997), On storm weakening during substorm expansion phase, Ann. Geophys., 15, 211.

Stüdemann, W., et al. (1987), The May 2-3, 1986 magnetic storm: First energetic ion composition observations with the Mics instrument on Viking, Geophys. Res. Lett., 14(4), 455–458, doi:10.1029/GL014i004p00455.

Tsurutani, B., and W. Gonzalez (1987), The cause of high-intensity long duration continuous AE activity (HILDCAAs): Interplanetary Alfven wave trains, Planet. Space Sci., 35, 405– 412.

Tsurutani, B. T., et al. (2006), Corotating solar wind streams and recurrent geomagnetic activity: A review, J. Geophys. Res., 111, A07S01, doi:10.1029/2005JA011273.

Tsyganenko, N. A., and M. I. Sitnov (2005), Modeling the dynamics of the inner magnetosphere during strong geomagnetic storms, J. Geophys.Res., 110, A03208, doi:10.1029/2004JA010798.

Valek, P., P. C. Brandt, N. Buzulukova, M.-C. Fok, J. Goldstein, D. J. McComas, J. D. Perez, E. Roelof, and R. Skoug (2010), Evolution of low altitude and ring current ENA emissions from a moderate magnetospheric storm: Continuous and simultaneous TWINS observations, J. Geophys. Res., 115, A111209, doi:10.1029/2010JA015429.

Wahba, Grace (1990), Spline Models for Observational Data, Society for Industrial and Applied Mathematics, Philadelphia.

Zhang, J.-C., M. W. Liemohn, M. F. Thomsen, J. U. Kozyra, M. H. Denton, and J. E. Borovsky (2006), A statistical comparison of hot-ion properties at geosynchronous orbit during intense and moderate geomagnetic storms at solar maximum and minimum, J. Geophys. Res., 111, A07206, doi:10.1029/2005JA011559.

Zhang, J., et al. (2007), Understanding storm-time ring current development through data-model comparisons of a moderate storm, J. Geophys. Res., 112, A04208, doi:10.1029/2006JA011846